ADVANCED MATERIALS AND FABRICATION METHODS
FOR
ORGANIC SOLAR CELLS

By

KANGMIN WU, B.Eng.

A Thesis

Submitted to the School of Graduate Studies

In Partial Fulfillment of the Requirements

For the Degree

Master of Applied Science

McMaster University

MASTER OF APPLIED SCIENCE (2010)...............McMaster University

(Materials Science & Engineering)............................Hamilton, Ontario

TITLE: Advanced materials and fabrication methods for organic solar cells

AUTHOR: Kangmin Wu, B.Eng. (Tongji University)

SUPERVISOR: Professor Igor Zhitomirsky

NUMBER OF PAGES: X, 101

Abstract

New electrochemical deposition methods have been developed for the fabrication of advanced composite coatings for organic solar cells and hybrid organic solar cells. The methods are based on electrodeposition of conjugated polymers and composites. In this work, poly[3-(3-N,N-diethylaminopropoxy)thiophene] (PDAOT) and poly(9,9-bis(diethylaminopropyl)fluorine-co-phenylene) (PDAFP) were used as electron donors. Single walled carbon nanotubes (SWNTs), ZnO and TiO_2 were used as electron acceptors. Also co-deposition of PDAOT and PDAFP has been developed in order to broaden the absorption range.

An electrophoretic deposition (EPD) method has been developed for the deposition of nanostructured ZnO and TiO_2 films. The stabilization and charging of the nanoparticles in suspensions was achieved using organic molecules, such as dopamine and alizarin yellow (AY) dye, which were adsorbed on the oxide nanoparticles. The adsorption mechanism is based on the complexation of metal ions at the surfaces of oxide nanoparticles. Cationic dopamine additive was used for the formation of deposits by cathodic EPD. The adsorption of anionic AY on the oxide nanoparticles resulted in charge reversal and enabled the formation of anodic deposits. The method enabled the co-deposition of ZnO and TiO_2 and the formation of composite films.

Electrophoretic deposition (EPD) method has been developed for the fabrication of TiO_2 films. Benzoic acid and phenolic molecules, such as 4-hydroxybenzoic acid, 3,5-dihydroxybenzoic acid, gallic acid, salicylic acid and salicylic acid sodium salt were investigated as charging additives for the EPD of TiO_2 particles. The deposition yield has been studied as a function of the additive concentration and deposition time for cathodic deposits obtained from the suspensions, containing benzoic acid, 4-hydroxybenzoic acid, 3,5-dihydroxybenzoic acid and anodic deposits prepared from the suspensions, containing gallic acid and salicylic acid sodium salt. The results obtained for the phenolic molecules with different number of OH groups were analyzed and compared with corresponding experimental data for benzoic acid without OH groups. The adjacent OH groups, as well as adjacent OH and COOH groups bonded to the aromatic ring of the phenolic molecules were beneficial for adsorption of the molecules on oxide particles. The adsorption mechanisms involved the interaction of COOH groups and OH groups of the organic molecules with metal ions on the particle surfaces and complexation.

The functional dispersants investigated in this work can be utilized for dispersion and functionalization of the nanoparticles and fabrication of hybrid large area organic solar cells. The new deposition method can be applied for the fabrication of dye-sensitized solar cells.

Acknowledgement

I would like to express my gratitude to all those who gave me the possibility to complete this thesis.

First of all, I would like to express my sincere appreciation to my supervisor, Professor Igor Zhitomirsky, whose help, stimulating suggestions and encouragement helped me in all the time of research and writing of this thesis.

Also I would give many thanks to all the team members, Yingying Li, Rong Ma, Chao Shi, Xin Pang and Yaohui Wang for their kindness and friendship.

Last but not the least; I take this opportunity to express my profound gratitude to my beloved father for the moral support and patience during my study in Canada.

Table of Contents

List of Figures

List of Tables

1 Introduction

The finite supply of traditional fossil fuels (oil, natural gas, coal, etc.) underscores the urgency of searching for alternative energy sources. Nowadays the most important role is attributed to solar energetics. Solar energy is converted into electricity by means of solar cells. At present, solar cells are mainly based on inorganic semiconducting materials, crystalline and amorphous silicon being the most important among them. However, silicon solar cells are not widely used thus far. The reason is that silicon photovoltaic technology is very complex, resulting in high cost of silicon solar cells. In the United States and Europe, the current cost of 1 kW/h of energy provided by solar cells is about \$ 0.30. This is two to five times higher than the cost of 1 kW/h of energy delivered to the population from traditional sources (thermal and nuclear power plants).

Organic solar cells are being extensively studied worldwide since they have the potential to inexpensively produce electricity from solar energy. According to calculations, 1 kW/h of electricity produced by organic solar cells should cost \$ 0.01–0.02 [1]. The flexibility is another important advantage of organic solar cells.

However, the method for the fabrication of organic layers of organic solar cells is still a big problem. Usually people use spin-coating, drop casting and vapor phase deposition. Each method has certain drawbacks. In our work, electrodeposition method was used, which can overcome most of the disadvantages of other methods. The major challenge is to electrodeposit conjugated polymers, which, in most cases, are electrically neutral. Another challenge is to avoid particle agglomeration during the deposition of polymer and metal oxide particle composites. The possibility to form large surface area films by electrodeposition is important for the separation of the excitons generated after the absoption of the photons from sunlight.

The subject of my research thus involves the development of advanced materials and deposition techniques for the fabrication of organic solar cells and the development of surface modification and electrodeposition of semiconductor nanoparticles using functional dispersants.

2 Literature Review

2.1 Solar Cells

A solar cell or a photovoltaic cell is a device that can convert light energy into electricity directly. Sometimes the term solar cell is reserved for devices intended specifically to capture energy from sunlight, while the term photovoltaic cell is used when the light source is unspecified.

Fundamentally, only two functions need to be fulfilled in solar cells: photogeneration of charge carriers (electrons and holes) in a light absorbing material, and separation of the charge carriers to a conductive contact that will transmit the electricity. This conversion can be briefly summarized as the photovoltaic effect.

Solar cells have many applications, and they have long been used in situations where electrical power from the grid is unavailable, such as in remote area power system, Earth-orbiting satellites and space probes, consumer products, e.g. handheld calculators or wrist watches, remote radiotelephones and water pumping applications. More recently, they are starting to be used in assemblies of solar modules (photovoltaic arrays) connected to the electricity grid through an inverter, often in combination with a net metering arrangement.[2]

2.1.1 Crystalline silicon cells

The majority of solar cells fabricated to date have been based on silicon in monocrystalline or large-grained polycrystalline form since 1954 and over 85% solar cells fabricated in 2009 were based on silicon.[3] The reason why silicon is so dominant is because silicon is a semiconductor with a well-balanced set of electronic, physical and chemical properties.

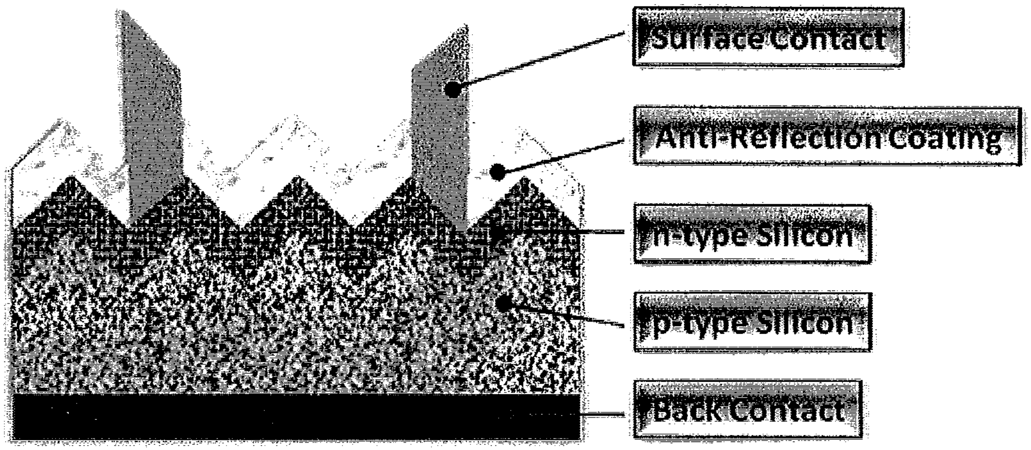

Figure 2-1 Basic structure of a silicon based solar cell

A complete crystalline silicon solar cell, as shown in Figure 2-1, consists of five layers. The first layer is called the surface contact, which, contacts the n-type silicon, transmitting the electrons to the appliance. In other words, the surface contact layer is also known as the electron collector electrode. Usually, when a photon hits a piece of silicon, one ofthree things may happen: 1.The photon goes straight through the silicon. 2. The photon reflects off the surface. 3. If the photon energy is higher than the silicon band gap value, the photon is absorbed by the silicon and that generates an electron-hole pair and heat. The anti-reflection coating is developed for preventing the photons from being reflected. Therefore, the coating is used in order to increase the number of photons which can reach the p-type silicon. The p-n junction is the most important part in the crystalline silicon solar cell and it is made of n-type silicon and p-type silicon. Electrons jump to the conduction band by absorbing photons which is higher than the bandgap of silicon and leave holes behind in p-type silicon. Following the previous step, electrons diffuse through n-type silicon and reach the electron collector electrode while holes diffuse through p-type silicon and reach the collector electrode, the back contact. By transferring through a external circuit, electrons and holes are re-combined and coverts solar energy into a usable amount of DC electricity.[4]

Crystalline silicon devices are approaching the theoretical limiting efficiency of 29%[5] and achieve an energy payback period of 1–2 years.[6]

2.1.2 Thin film solar cells

Although silicon solar cells can acquire high energy transfer efficiency, the problem of high cost of silicon was recognized right from the beginning, and, it has also been recognized that cheaper solar cells can be produced only if cheaper materials and lower cost technologies are utilized. Thus, thin film cells were introduced.

A thin film solar cell is a kind of solar cell that consists of one or several layers of different photovoltaic materials in thin-film form onto a substrate. The structural, chemical and physical properties are strongly dependent on a large number of deposition parameters and thickness, which may encompass a considerable range, varying from a few nanometers to even tens of micrometers.

In general the thin film solar cell consists of substrate, TCO (transparent conducting oxide), window layer (p or n-type), absorber layer (i or p type) and metal contact layer.[7]

2.1.2.1 Cadmium telluride solar cells

Cadmium telluride solar cell, which is based on the use of a cadmium telluride thin film layer to absorb sunlight, is the first and only thin film photovoltaic technology to surpass crystalline silicon in cheapness for a significant portion of the PV market.[8] The structure is shown in Figure 2-2.

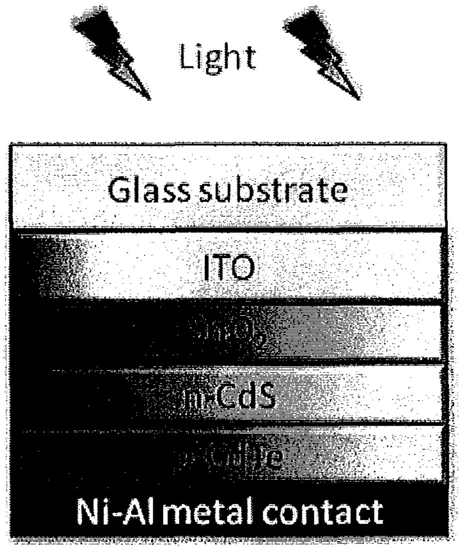

Figure 2-2 Structure of a cadmium telluride solar cell

On account of its optoelectronic and chemical properties, CdTe is an ideal absorber material for high efficiency, low cost thin film solar cells. CdTe has a direct bandgap of 1.5 eV, and an absorption coefficient ~10^5/cm in the visible region, which indicates that a layer with a thickness of a few micrometers is sufficient to absorb ~90%

of the incident photons. Owing to the high ionicity (72%) of CdTe, the formed crystallite is well-passivated and strong chemical bonding (5.75 ev) results in high chemical and thermal stability. A large variety of fabrication methods can be used for CdTe solar cells such as close-spaced sublimation (CSS), PVD, electrodeposition, screen-printing and all of these techniques may produce a device with efficiency >10%.

The solar cells based on CdS/CdTe junction have achieved an efficiency 16.5% in small areas compared with the theoretical maximum efficiency of 29%.[9, 10]

2.1.2.2 Copper indium gallium diselenide solar cells (CIGS)

CIGS is a I-III-VI compound semiconductor material, which may have some very desirable properties for photovoltaic application, composed of copper, indium, gallium, and selenium. The material is a solid solution of copper indium selenide (often abbreviated "CIS") and copper gallium selenide. The structure of CIGS is shown in Figure 2-3.

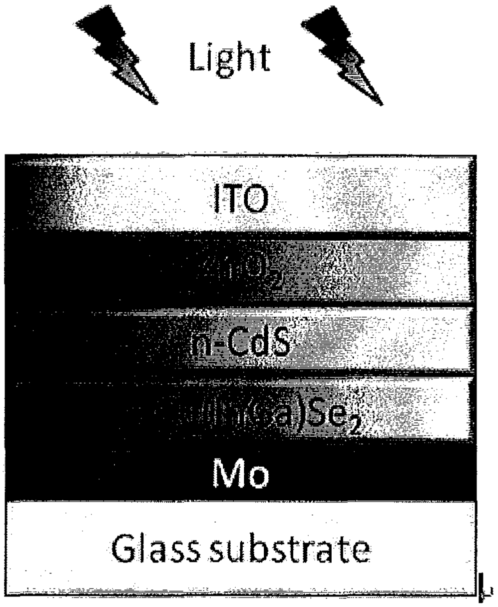

Figure 2-3 Structure of a copper indium gallium diselenide solar cell

$CuInSe_2$, with bandgap of 1 eV, is considered to be an ideal material for photovoltaic applications. It is one of the most absorbing semiconductor materials with an absorption coefficient of $3\text{-}6\times10^5$/cm. The most benevolent feature of polycrystalline $CuInSe_2$ is its electrically benign nature of its numerous structural defects and hence polycrystalline $CuInSe_2$ films are as good an electronic material as its single-crystal counterpart. An efficiency of 15.4% has been achieved from $CuInSe_2$ devices.[11] Alloying with Ga increases the bandgap of $CuInSe_2$ so as to make it more suitable for high-efficiency single-junction and multijunction devices.[12] An increase in the bandgap and improved process conditions resulted in the fabrication of high-performance solar cells with efficiencies of 19.2%.[13] Although the efficiency and stability of $Cu(InGa)Se_2$ solar cells are promising, still there are several factors that are less favorable for large-scale production of such devices. The components alloyed with $CuInSe_2$ makes the processes extremely complex and thus intelligent processes are required for precise control during deposition. Expensive and rare metals such as In and Ga do add to the cost of manufacturing.

2.1.2.3 Dye-sensitized solar cells (DSSC)

A dye-sensitized solar cell is an emerging technology that applied in low-cost solar cells. It is based on a semiconductor formed between a photo-sensitized anode and an electrolyte, a photo-electrochemical system.

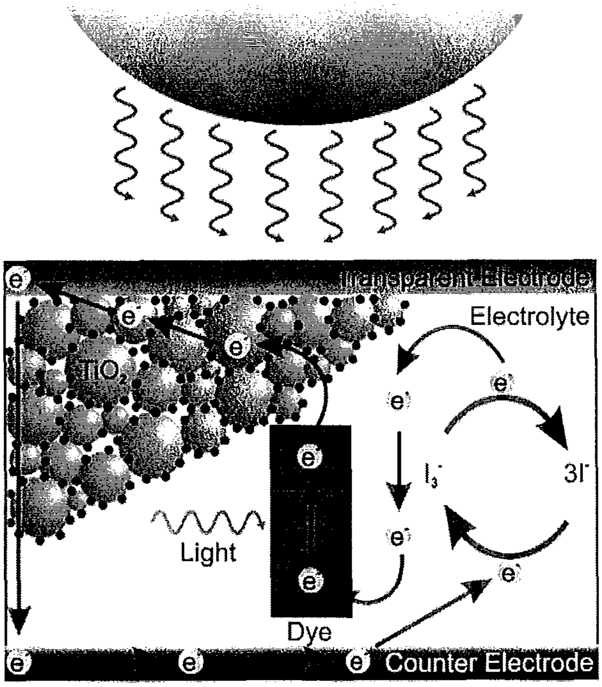

Figure 2-4 Schematic illustration of a generic dye-sensitized solar cell[14]

A DSSC is composed of a porous layer of titanium dioxide nanoparticles, covered with a molecular dye that absorbs sunlight, which has typically been a ruthenium metalorganic dye (Ru-centered). A Dye-sensitized TiO2 solar cell is one of the successful combination of materials, usually consisting of a dye-sensitized nanocrystalline TiO_2 film, an electrolyte with an I^-/I_3^- redox couple and a Pt counter-electrode. Electricity is generated in the DSSC via the following steps (as shown in Figure 2-4):

1. Incident light results in excited state dye D*. $D \rightarrow D^*$
2. Electron transfers from D* to conduction band. $D^* \rightarrow D^+ + e^-$
3. Electron passes through circuit. $e^-(WE) \rightarrow e^-(CE)$ + electricity
4. Reductor is regenerated. $Ox + e^- \rightarrow Red$
5. Dye is regenerated. $Red + D^+ \rightarrow Ox + D$

Although the highest efficiency for current DSSCs is about 11%,[15, 16] there are still some problems related to DSSCs, such as degradation, difficulties in manufacturing large-scale DSSCs. Both might limit the use of DSSCs.

2.1.2.4 Organic solar cells

Recently, a new world record of 8.13% was made by Solarmer Energy, Inc. for its organic photovoltaic cell efficiency in 7.27.2010, certified by the National Renwable Energy Laboratory (NREL)[17]. At present, organic solar cells are being extensively studied worldwide since they have the potential to inexpensively produce electricity from solar energy.

These cells are different from inorganic semiconductor solar cells in that they do not rely on the large built-in electric field of a p-n junction to separate the electrons and holes created when photons are absorbed.

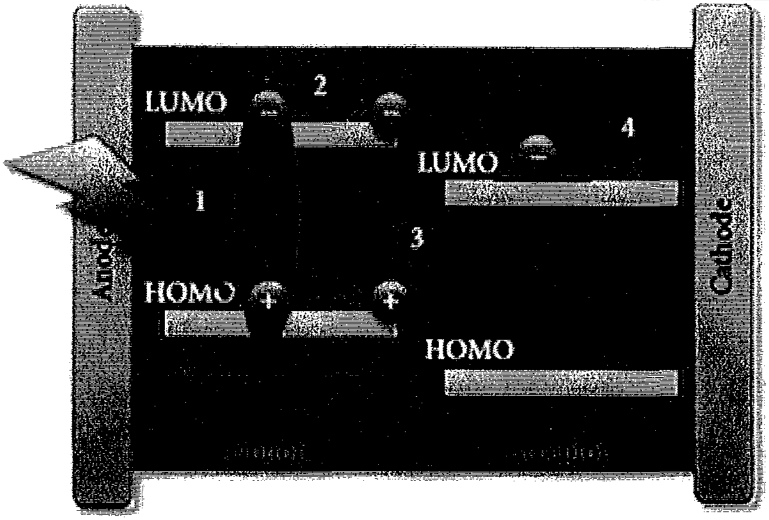

Figure 2-5 Scheme of operative sequence of an organic solar cell[18]

As is shown in Figure 2-5, the generation of photocurrent is a cascade of four steps. When the organic layer (called the active layer) absorbs light, electrons will be excited to LUMO (lowest unoccupied molecular orbital) and forms excitons while holes are left in HOMO (highest occupied molecular orbital). The exciton diffuses inside the material to reach the donor-acceptor interface where it will be separated, and then free charges diffuse through the layer and collected by the electrodes. The separation between HOMO and LUMO is considered to be the band gap of organic electronic materials. The band gap is typically in the range of 1-4 eV.[19]

Organic solar cells are flexible, while classical electronics is dominated by the use of rigid and brittle structures, which is determined by the physical properties of inorganic materials. Such cells can be integrated into clothing, facial coatings, and packaging.[20] In addition, they are light weight, and able to generate electricity with a comparative low cost from the sun. However, organic solar cells also suffer from problems of degradation and low power conversion efficiency.

2.1.3 Multi-junction solar cells

With a maximum efficiency of 41.6%, multi-junction solar cells are currently the most efficient solar cells.[21] In fact, multi-junction solar cells have the highest theoretical limit of 86.8% conversion efficiency compared to any other photovoltaic technologies.[22-24]

The fundamental difference between multi-junction solar cells and crystalline silicon solar cells is that there are several p-n junctions connected in series instead of one as shown in Figure 2-6(b). In order to better cover the solar spectrum AM1.5 (terrestrial reference spectrum for photovoltaic performance evaluation), suitable photovoltaic materials with different bandgaps should be carefully chosen for each p-n junction. Multi-junction solar cells consist of some single-junction solar cells stacked upon each other, so that each layer going from top to bottom has a smaller bandgap than the previous, and so it absorbs and converts the photons that have energies greater than the bandgap of that layer.[25] Photons of different wavelength $\lambda = \frac{hc}{eE_g} \approx \frac{1.24\times10^{-6}}{E_g}$ are absorbed with the significantly different bandgaps of different materials. Thus, triple-junction solar cells currently in production are made of InGaP (1.86 eV), InGaAs (1.4 eV), and Ge (0.65 eV), which is shown in Figure 2-6.[26]

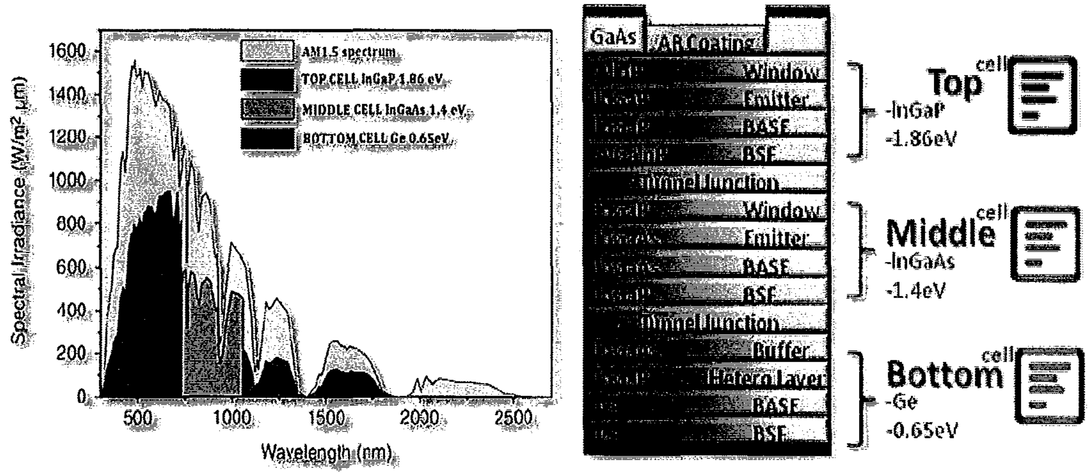

(a) (b)

Figure 2-6 (a) Graph of Spectral Irradiance G as a function of wavelength λ which shows the covering of the solar spectrum AM1.5[27] (b) The structure of a multi-junction solar cell. There are six important types of layers: p-n junctions, BSF layers, Window layers, tunnel junctions, AR coating and metallic contacts.

Due to the high cost of the complex structure and the high price of materials used in multi-junction solar cells, light concentrators are used in this system. This is because with light concentrators under illumination of at least 400 suns, the use of multi-junction solar panels may become possible and profitable.[28]

2.2 Characterization of an organic solar cell device

A solar cell device is characterized by its current-voltage curve, which is measured under standard AM1.5 illumination conditions by using a solar simulator. The standard light power density is standardized at 1000mW/cm^2 with a spectral intensity distribution matching that of the sun on the earth surface at an incident angle of 48.2°. [29]

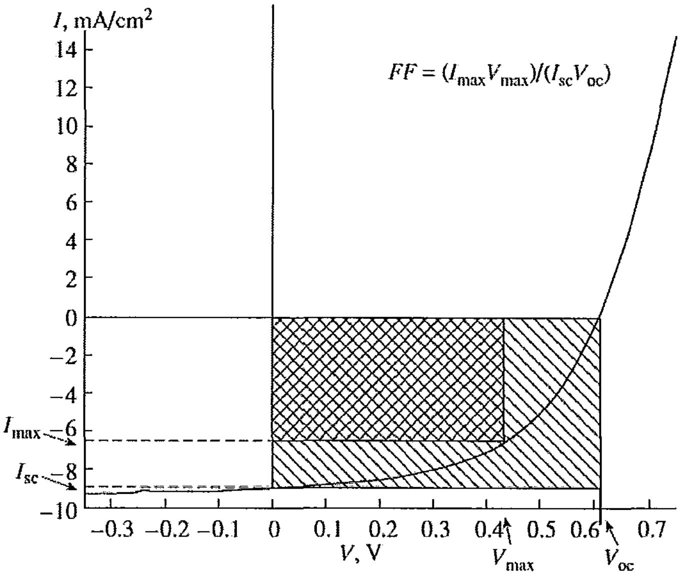

Figure 2-7 Typical current–voltage curve of a photovoltaic cell[20]

Three basic parameters of a photovoltaic cell can be determined from the light current–voltage characteristics: open circuit voltage (V_{oc}), short circuit current (I_{sc}), and fill factor (*FF*). Figure 2-7 shows a typical current-voltage curve of a photovoltaic cell. The short circuit current density is determined at zero applied voltage. The voltage that should be applied to compensate for the emf of the cell is referred to as the open circuit voltage (V_{oc}). The maximal energy point, which can be acquired by taking out the maximum point of the multiplied coordinates of the curve in the fourth quadrant, determines the actual efficiency of a photovoltaic cell. The current and voltage at this point are designated as $I=I_{\max}$ and $V=V_{\max}$. The power conversion efficiency η of a photovoltaic cell is calculated by the following formulas:

$$\eta\% = \frac{P_{el}}{P_{light}} = \frac{V_{max}I_{max}}{P_{light}} = \frac{V_{oc}I_{sc}FF}{P_{light}} \qquad (2\text{-}1)$$

Where P_{light} is the power of the incident light from an external light source, and P_{el} is the electricity generated by the photovoltaic cell. *FF* is the proportionality coefficient called the fill factor. Graphically, the fill factor is the ratio of the area of the rectangle with sides I_{max} and V_{max} to the area of the rectangle with sides I_{sc} and V_{oc}. [20]

2.2.1 Open circuit voltage

Generally, the open circuit voltage of a metal-insulator-metal (MIM) device is determined by the difference in work function of the two metal contacts.[30] However, the maximum available voltage in a p-n junction device is determined by the difference of the quasi Fermi levels of the two charge carriers, that is, n-doped semiconductor energy level and p-doped semiconductor energy level respectively. While in organic solar cells, the open circuit voltage is found to be linearly dependent on the highest occupied molecular orbital HOMO level of the donor (p-type semiconductor quasi Fermi level) and lowest unoccupied molecular orbital LUMO level of the acceptor (n-type semiconductor quasi Fermi level).[31, 32] The open circuit potential is a sensitive function of energy levels of the used materials as well as their interfaces.[33, 34]

2.2.2 Short circuit current

In the ideal, loss free contacts, the short circuit current - I_{sc}, is determined by the product of the photoinduced charge carrier density and the charge carrier mobility within the organic semiconductors:

$$I_{sc} = ne\mu E \tag{2-2}$$

where n is the density of charge carriers, e is the elementary charge, μ is the mobility, and E is the electric field. Assuming 100% efficiency for photoinduced charge generation in a bulk heterojunction mixture, n is the number of absorbed photons per unit volume.

For a given absorption profile of a photovoltaic material, the bottleneck is the mobility of charge carriers. Mobility is not a material parameter but a device parameter. It is sensitive to the nanoscale morphology of the organic semiconductor thin film.[35-37] The film nanomorphology depends on the preparation method and condition. Parameters such as solvent type, the solvent evaporation (crystallization) time, the temperature of the substrate, and the deposition method can change the nanomorphology.[38, 39]

2.2.3 Fill factor

Fill factor is determined by charge carriers reaching the electrodes, when the built-in field is lowered toward the open circuit voltage. Actually, there is a competition between charge carrier recombination and transport. Hence, the product of the lifetime τ times the mobility μ determines the distance d that charge carriers can drift under a certain electric field E:

$$d = \mu\tau E \tag{2-3}$$

This product $\mu\tau$ has to be maximized.[40] Furthermore, the series resistances influence the filling factor considerably and should be minimized. Finite conductivity of the ITO substrate clearly limits the FF of large area solar cells.[41] Finally, the device should be free of "shorts" between electrodes to maximize the parallel shunt resistance.

2.2.4 External quantum efficiency

External quantum efficiency is another important parameter for solar cell characterization. It is a quantity defined for a photosensitive device as the percentage of photons hitting the photoreactive surface that will produce an electron–hole pair. It is an accurate measurement of the device's electrical sensitivity to light. Since the energy of a photon depends more precisely on its wavelength, external quantum efficiency is often measured over a range of different wavelengths to characterize a device's efficiency.

It is calculated by the number of electrons extracted in an external circuit divided by the number of incident photons at a certain wavelength under short-circuit condition.

$$\mathrm{EQE}(\lambda) = \frac{number\ of\ electrons}{number\ of\ photons} = \frac{I_{SC}(\lambda)/e}{P_{light}(\lambda)e\lambda} \qquad (2\text{-}4)$$

λ is the wavelength, e is the elementary charge.

2.3 Architecture of an organic solar cell

All described configurations of organic photovoltaic cells can be divided into four groups: single layer cells, in which the organic electronic material is deposited between the two metallic conductors, bilayer cells, in which layers of photoactive components are deposited over one another; bulk heterojunction cells, in which the donor and acceptor are blended in a single photoactive layer, tandem cells, in which there are two or more cells sitting atop one another (arranged in stacks). These types of cells differ not only in structure, but also in materials and manufacturing processes.

2.3.1 Single layer cells

In its simplest form, an organic solar cell consists of a single polymer layer sandwiched between two different electrode materials as depicted in Figure 2-8. Conjugated π-systems are extensively used as both donor and acceptor materials. Usually, a layer of indium tin oxide (ITO) with high work function serves as the hole collector and a layer of low work function metal such as Al, Mg and Ca is worked as an electron collector. Photons can reach the cell through the transparent contact (ITO) and excitons are created when photons are absorbed in the organic film. The electric field separates the electrostatic bonds of excitons and then moves electrons to the positive electrode and holes to the negative electrode. Generally, not all of the photons will be absorbed in the organic active layer. Some will be reflected by the back metal contact and may have another chance to be absorbed in the layer before leaving the device through the ITO layer. Usually the thickness of the organic layer is between 40 and 200 nm.

Figure 2-8 Structure of a single layer organic solar cell

A survey of the photovoltaic performance of various single layer materials is given in Table 2-1.

PCE	V_{oc}	FF	Device	Year
0.5%	1V	23%	Al/PPV+PEDOT/ITO	1998[42]
0.1%	0.7V	25%	Al/THPF/ITO	2000
0.1%	0.1V	25%	Al/THPF/ITO	2000
0.09%	0.5V	27%	Al/CN-MEH-PPV/ITO	1997[43]
0.07%	0.7V	25%	Al/MEH-PPV/ITO	2000[44]

Table 2-1 Survey of important performance parameters of various organic single layer solar cells.[45]

From the table, it can be seen that single layer organic photovoltaic cells do not work well. Most all of them have low power conversion efficiencies lower than 0.5%. The main losses in single layer structures are due to the short exciton diffusion lengths and recombination of the excited charge carriers. The electrons often recombine with the holes in the organic layer rather than reach the electrode. Another problem is that the electric field resulting from the difference between the two conductive electrodes is not sufficient to break up the photogenerated excitons. In order to solve this problem, the multilayer organic photovoltaic cells were developed.[46]

2.3.2 Bilayer cells

The bilayer organic solar cells were historically the first photovoltaic organic cells that showed an acceptable power conversion efficiency of about 1%. Generally, conjugated polymers have relatively high hole mobilities but low electron mobilities. This intrinsic imbalance in carrier mobility can be overcome by the incorporation of an n-type semiconductor material as electron acceptor to provide a pathway for electron transport.

C.W. Tang in 1980–1987 modeled p – n junctions based on organic semiconductors that consist of metal phthalocyanine (p-type)/perylene derivative (n-type) and made it possible to convert light into electricity with a power conversion efficiency of about 1%.[47] Since then, many studies dealing with the photovoltaic properties of such systems have been published.

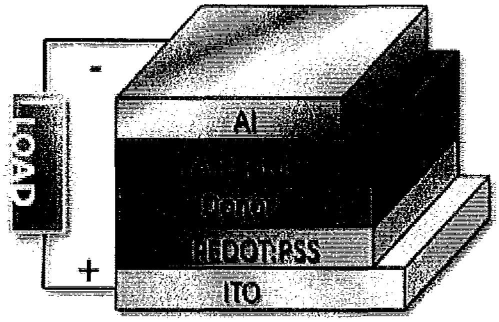

Figure 2-9 Structure of a bilayer organic solar cell

Figure 2-9 shows a bilayer organic solar cell. In a bilayer device, p-type and n-type semiconductors are sequentially stacked on top of each other. In other words, the p-type organic semiconductor is served as an electron donor while the n-type semiconductor is served as an electron acceptor. With the introduction of an electron acceptor layer between the active material and the negative electrode, both the exciton diffusion range and the poor shunt resistor can be improved. Such bilayer devices using organic semiconductors were realized for many different material combinations. The conducting polymer poly(3,4-alkenedioxythiophenes):poly(styrenesulfonate) (PEDOT:PSS) is usually used as an anode buffer material for smoothing the ITO surface, enhancing the adhesion to the upper light absorbing layer, and improving the device stability by hindering oxygen and indium diffusion through the anode.[48, 49]

A survey of the photovoltaic performance of various polymer-polymer bilayer solar cells is given in Table 2-2.

PCE	V_{oc}	FF	Doner/Acceptor	Year
1.5%	1.1V	50%	PPV/BBL	2004[50]
1.4%	1.4V	34%	MDMO-PPV:PF1CVTP/PF1CVTP	2006[51]
1.3%	1.3V	31%	M3EH-PPV/CN-Ether-PPV	2006[52]
1.1%	0.9V	47%	MEH-PPV/BBL	2004[50]
0.6%	1.5V	23%	M3EH-PPV/CN-PPV-PPE	2006[52]

Table 2-2 Survey of important performance parameters of various polymer bilayer solar cells[45]

Although great progress was achieved by the polymer-polymer bilayer devices, the power conversion efficiency is still limited for the following reasons. A polymer layer needs a thickness of no less than 100 nm to absorb enough light. Only a small fraction of the excitons can reach the heterojunction interface with such a large thickness of the polymer layer since the diffusion length of excitons in organic electronic materials is typically between 10-15 nm. On the other hand, the dissociation efficiency is also quite low. Later on, a new architecture known as the bulk heterojunction photovoltaic solar cell was designed to address the problem.

2.3.3 Bulk heterojunction cells

The bulk heterojunction photovoltaic solar cell is currently the focus of intense research worldwide. With an active layer consisting of a mixture of donor and acceptor materials, Shaheen et al. showed that a power conversion efficiency of 2.5% under AM

1.5 conditions can be obtained.[53]

Currently, the best materials for organic bulk heterojunction solar cells are fullerene compounds (acceptor) and poly-conjugated polymers (donor). Other combinations of materials have also been studied. However, high power conversion efficiencies are, as a rule, achieved only with fullerene compounds until now. Figure 2-10 shows a basic structure of an organic bulk heterojunction photovoltaic device.

Mainly there are three main advantages of the bulk heterojunction cell that was developed. First, the active layer in the bulk heterojunction device can be considerably thicker than the sum of the exciton diffusion lengths in the donor and acceptor material as long as the layer comprises an interpenetrating network, which can absorb more photons from the light. Second, in the bulk heterojunction cell, the contact area between the donor and acceptor phase is generally many orders of magnitude larger than in bilayer cells which leads to a nearly 100% photoinduced charge separation in the active layer. Third, the materials used for their manufacture are usually readily soluble in organic solvents and

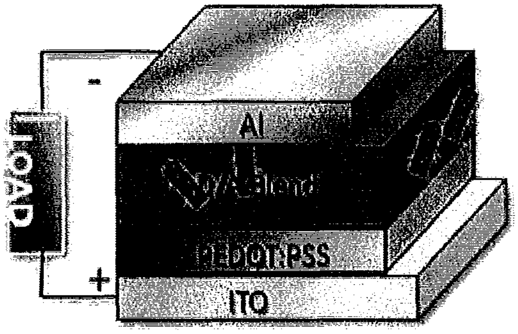

Figure 2-10 Structure of a bulk heterojunction organic solar cell

can be applied from solution. Deposition from solution makes it possible to reduce expenses in producing devices with the use of modern printing technologies.

PCE	V_{oc}	FF	Doner/Acceptor	Year
3.0%	0.8V	51%	MDMO-PPV/ $PC_{71}BM$	2003[54]
4.4%	0.9V	67%	P3HT/PCBM	2005[55]
4.9%	0.6V	54%	P3HT/PCBM	2005[56]
5.0%	0.6V	68%	P3HT/PCBM	2005[57]

Table 2-3 Best in class solar cells: Blends of polymers and fullerene derivatives[45]

Although Table 2-3 shows a comparably higher power conversion efficiency compared to bilayer solar cells, the device efficiency is still limited due to two main factors. First the open circuit voltage reaches only 0.7 V, which is quite small compared to the bandgap of P3HT (1.9 eV). The second factor limiting the efficiency of P3HT:PCBM cells is the absorption range of P3HT. P3HT absorbs visible light until about 650 nm, meaning that most of the red portion of the visible spectrum and all infrared photons cannot be harvested.[45]

2.3.4 Tandem cells

Since it seems unlikely that a single organic junction can absorb efficiently from the blue to the infrared region, tandem structures were proposed, where different subcells absorb different wavelength regions.

Tandem photovoltaic cells are those in which there are two or more subcells sitting atop one another (arranged in stacks), which are formally connected in series since they have a shared electrode that functions as the cathode for one cell and the anode for the other as depicted in Figure 2-11.

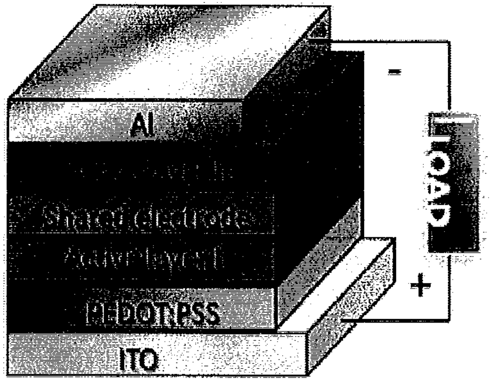

Figure 2-11 Structure of a tandem organic solar cell

At the output of the tandem cell, the short circuit current is equal to the minimal current among those of the constituent subcells (optimally, these currents should be equal) and the open circuit voltage is equal to the sum of the voltages of the constituent subcells. Therefore, one difficulty in designing tandem solar cells is that the current of each subcell has to be matched in order to achieve the highest efficiency, since the total current in the device is limited by the lowest current generating subcell.

For the tandem cells based on polyconjugated polymers and fullerene compounds, power conversion efficiencies of about 6.5% have been achieved.[58]

2.4 Materials selection in each process in bulk heterojunction organic solar cells

After the discovery in 1991 that the transfer of photoexcited electrons from conjugated polymers to fullerenes is very efficient, it took 10 years more until organic solar cells reaching 2.5% efficiency were reported.[59, 60]

The process of conversion of light into electricity by an bulk heterojunction organic solar cell can be described as a cascade of four steps: absorption of a photon leading to the generation of electrically neutral bound electron-hole pairs, diffusion of excitons to the heterojunction interface of the donor and acceptor material, dissociations of the excitons into free carriers, and transport of these carriers to the respective electrodes. These steps are outlined in Figure 2-5. The donor materials have a smaller LUMO and HOMO compared with the acceptor. In this regard, the donor is the hole transporting material and ideally makes ohmic contact with the anode while the acceptor materials transport electrons and contact the cathode.

The absorption efficiency (η_A) is largely controlled by the UV-absorption spectrum of the active layer which consists of the donor and the acceptor, as well as its thickness. The efficiency (η_{ED}) of the second process, which is known as the exciton diffusion, is determined by the exciton diffusion length (L_D) and the morphology of the DA (donor and acceptor) interface. The process of exciton dissociation into free charges is characterized by the efficiency (η_{ct}) that is large if energetically favourable. The percentage of the dissociated excitons collected at the electrodes is characterized by the charge collection efficiency (η_{cc}), which is sensitive mainly to the morphology and mobility of the active layer. Then, the overall efficiency of converting incident photons to electrical current, or the external quantum efficiency (η_{EQE}), can be calculated via:

$$\eta_{EQE}(\lambda, V) = \eta_A(\lambda)\eta_{ED}\eta_{CT}(V)\eta_{CC}(V) \qquad (2\text{-}5)$$

Here, λ is the wavelength of incident light, and V is the voltage across the cell.[61]

2.4.1 Absorption

Conjugated π-systems are extensively used as both donor and acceptor materials. The strength and width of the absorption spectrum of an active layer of bulk heterojunction solar cell determines to a large extent its potential for harvesting incident solar radiation. They are intrinsically different from crystalline inorganic semiconductors that absorb a continuous spectrum of photons with energy greater than their bandgap and these inorganic semiconductors provide large carrier mobility with their three-dimensional rigid lattice. Organic semiconductors have well-defined electronic transitions which are typically quite narrow and a propensity to be very susceptible to the background. Furthermore, since the thickness of organic semiconductors has to be thin, because of short exciton diffusion lengths, the incident light cannot be captured in an efficient way.

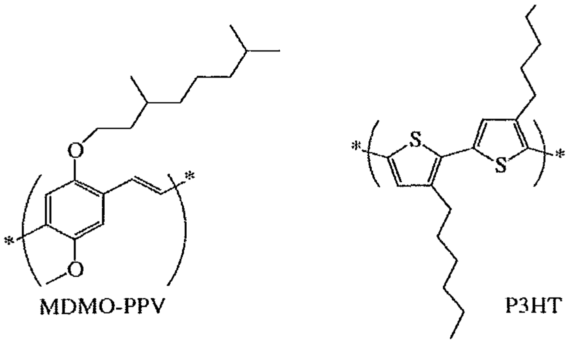

Figure 2-12 Molecular structure of MDMO-PPV and P3HT

The generated photocurrent density in organic solar cells depends primarily on the absorption spectrum of the active layer. Solar cells based on P3HT show a much higher efficiency than MDMO-PPV cells due to the difference in the absorption spectra of these donor materials. Their structures are depicted in Figure 2-12. MDMO-PPV absorbs light only up to 570 nm, whereas P3HT absorbs up to 670 nm. The difference in 100 nm causes a twofold increase in current density in going from MDMO-PPV cells to cells based on P3HT. This is due to the fact that the intensity of sunlight is maximal in the range 570–670 nm (Figure 2-12)[33].

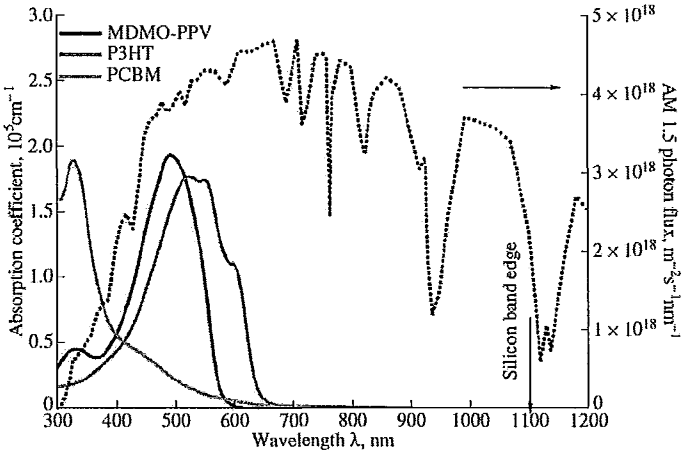

Figure 2-13 Absorption spectrum of the polymers MDMO-PPV, P3HT, and fullerene compound PCBM and the solar spectrum under AM1.5 (Air Mass 1.5) conditions.[62]

In addition, these optical transitions tend to be very sensitive to their surroundings. For example, the absorption of small molecules that also may act as electron donor materials in the system can be detected in the gas phase or in a very dilute solution, under where in the probability of the photon is determined by molecular interaction. When they are transited to the solid state, the tendency of a given molecule to aggregate can have significant impact on their absorption spectrum.

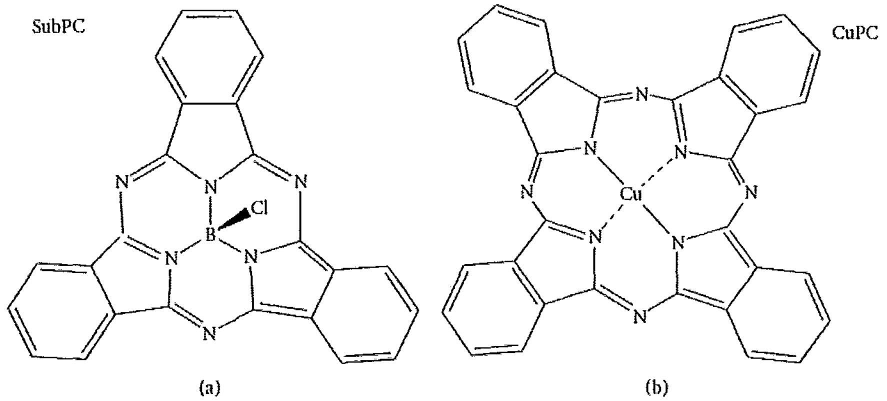

Figure 2-14 Molecular structure of SubPC and CuPC

Many papers reported SubPC and CuPC (Figure 2-14) as materials that can be used in organic solar cells. The absorption spectrum of these two molecules has similar profiles when recorded in very dilute solutions, while they are quite different in the solid state as shown in Figure 2-15 [61]

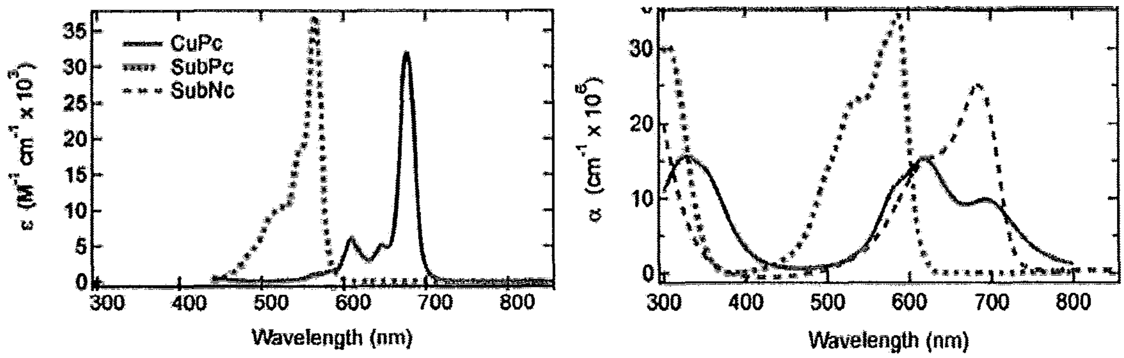

Figure 2-15 Molar absorptivities, *ε*, of CuPc and SubPc solutions (left) and absorption coefficients, *α*, of CuPc, SubPc, and SubNc thin films (right). For solution spectra, CuPc is in 1-methylnapthalene (8 × 10^{-5}M) and SubPc is in toluene (2.3 × 10^{-5}M).

The absorption spectrum of a thin film of SubPc is comparable to that of SubPc in solution while the CuPc spectrum recorded in solid state is quite different from the spectrum of CuPc in solution. This is mainly due to the fact that films made of CuPc show the presence of the aggregates of planar phthalocyanine molecules whereas SubPc forms an amorphous film.[63-67]

The crystalline films such as poly-(3-hexylthiophene) (P3HT) are better candidates for bulk heterojunction single-junction organic solar cells due to a wider absorption spectrum compared with amorphous films. Ideally, the absorption spectrum of such materials should extend to ~750-800 nm in order to capture more photons. In addition, the crystalline films have a higher charge carrier mobility that allows the active layer to be thicker, which is beneficial for large area devices.

Another alternative approach to extend the absorption spectrum is to use inorganic nanocrystals in organic solar cells leading to so-called hybrid solar cells.[68-70] Nanocrystals based on CdS, CdSe, CdTe, ZnO, SnO_2, TiO_2, Si, PbS and PbSe have been used so far as electron acceptors. By tuning the diameter of the nanocrystals, their band gap as well as their energy level can be varied based on the quantum size effect. Surface modification of nanocrystalline metal oxide particles with ligands can alter optical properties of nanoparticles.[71]

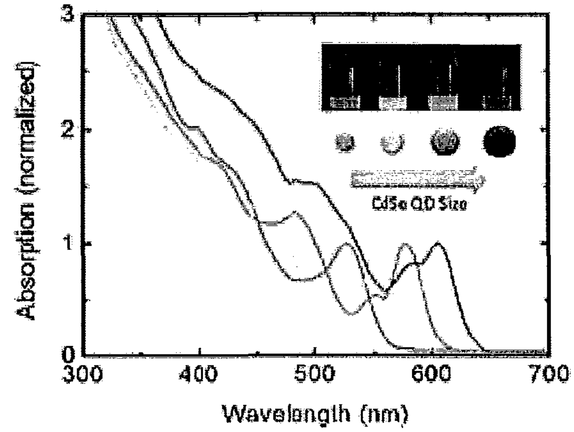

Figure 2-16 Absorption spectrum of CdSe quantum dots with different sizes. Inset: photoluminescence of differently sized quantum dots (3–6 nm) under UV irradiation.[72]

As shown in Figure 2-16, along with the increasing size of the CdSe nanocrystals from 3 nm to 6 nm, the band gap is reduced and it results in light absorption at longer wavelength. Quantum confinement leads to an enhancement of the absorption coefficient compared to that of the bulk materials.[73] Therefore, both components have the ability to absorb incident light in the nanocrystals/polymer system, while in the typical polymer/fullerene system the fullerene contributes very little to the photocurrent generation.[74] For example in blends containing 90 wt% CdSe nanoparticles in P3HT, about 60% of the total absorbed light energy can be attributed to P3HT due to the strong absorption coefficient.[75]

2.4.2 Exciton diffusion

Once the exciton is generated after absorption, the neutral electron-hole pair remains localized on a few polymer repeat units or a molecule and they are bound to each other by electrostatic attraction. The fraction of excitons that can reach the D/A interface is characterized by the exciton diffusion length (L_D) and the location at which an exciton is created with respect to the nearest dissociation centre. The fact that organic semiconductors possess low mobility puts significant constraints on the thickness of layers used in organic cells. Layers that have a thickness of 200 nm may not absorb significantly more photons than a thinner film but exhibit a larger resistance. Excitons that do not reach the D/A interface are lost for energy conversion and have no contribution to the photocurrent.

After adding a charge to a polymer chain, the chain will deform in order to reduce the energy of the carrier. Then a polaron is constituted by the charge and the deformation of the chain. Polarons can drift along the conjugated chain and once they reach the end of a conjugated segment, a hopping process to another conjugated chain can occur. It is known that in molecular crystals, excitons can diffuse efficiently by energy transfer and the same mechanism takes place in thin layers of molecular semiconductors.[76]

For most conjugated polymers, the exciton diffusion lengths are typically around 10-20 nm before recombination takes place.[77, 78]

Heremans et al. have found a way to increase the L_D by doping a small percentage of a phosphorescent because of the ability of efficiently capturing initially generated singlet excitons on the host and transform them into triplets. Generally these triplets have longer life time than singlet excitons.[61] In their account, the L_D of an SY/C_{60} D/A interface was increased from 4 nm to 9 nm after adding 5% PtOEP and correspondingly η_{ED} also increased.

Besides, the most-explored approach to date is to reduce the average distance between the D/A interface by forming a bulk heterojunction cell. However, the acceptor materials should be enough and be well dispersed for the excitons to reach the interface. This approach can be applied to solar cells produced by solution processing or thermal evaporation with η_{ED} approaching unity. The major disadvantage of the bulk heterojunction organic solar cells is the lack of direct control of the morphology of the active layer. Very fine morphologies may cause non-geminate bulk recombination of charge carriers. Therefore, as a general guideline, donors with larger exciton diffusion lengths will allow coarser morphologies and are preferred. The ideal bulk heterojuncton organic solar cell is probably the one that mimics an network structure composed of distinct donor and acceptor lamellae that can be achieved by nanoimprint technology[79]

2.4.3 Charge dissociation

When an exciton reaches a D/A interface, it is dissociated into a so-called geminate pair. This charge pair still has a binding energy that may be as high as 0.5 eV. Therefore, a subsequent dissociation step is required to acquire free charge carriers from initial excitons, with a global efficiency defined as η_{CT}. The nature of the geminate pair state and the conditions for efficient charge transfer are still under continuing research since it is difficult to determine the point where the geminate pair is totally dissociated.[80, 81]

Generally η_A and η_{ED} influence only short-circuit current (I_{SC}), and η_{CT} has important consequences to the open-circuit voltage (V_{OC}) and *FF*.[82-84] As depicted in Figure 2-14, the limiting value of V_{OC} for a D/A layer that allows the exciton to dissociate into free carriers completely is given by the difference between the HOMO of the donor ($HOMO_D$) and the LUMO of the acceptor ($LUMO_A$) minus at least the binding energy of the geminate pair at the D/A interface.[82]

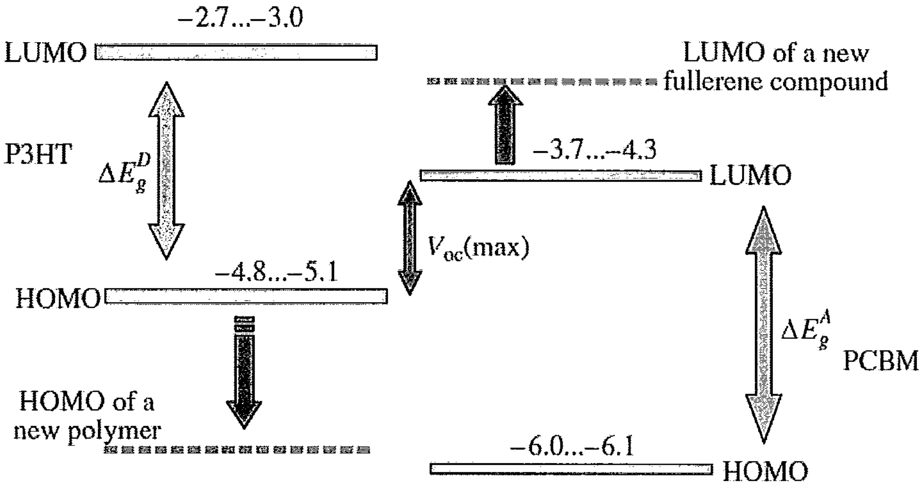

Figure 2-17 Scheme of the frontier orbitals of the P3HT/PCBM system.[20]

$$V_{OC}(\max) = E\,(\mathrm{LUMO_A}) - E(\mathrm{HOMO_D}). \quad (2\text{-}6)$$

For example, P3HT and PCBM are the D/A materials for organic photovoltaic cell. (Figure 2-17) The maximal value of V_{OC} for the P3HT/PCBM system is calculated as 0.8 V. The experimental V_{OC} values for P3HT/PCBM cells vary from 0.59 to 0.66 V, which is consistent with the theoretical values.[32] There are two ways to increase η_{CT} that largely depend on V_{OC}. The first method is to use another conjugated polymer with a lower HOMO energy and the LUMO energy should also be decreased. Otherwise with increasing $\Delta E^D{}_g$, the light absorption range will be decreased considerably that might lead to a slump of the η_A. Another way that can increase the value of η_{CT} is to increase the LUMO level of the acceptor material. For instance, the LUMO energy of fullerene compounds can be increased from –4.3 to –3.0 eV without loss in electron transfer efficiency. Such changes should lead to a nearly twofold increase in V_{OC} in the cells.[85] However, such a strong change in the electronic properties of acceptor materials is a very complicated chemical problem. Also, the band gap of inorganic metal oxide nanoparticle can be changed by using different surface ligands. However, both should be taken into considering that modified acceptor materials should have suitable electron transport properties.

2.4.4 Charge transfer and charge collection

Once dissociated, carriers need to diffuse through the materials and the collected by the respective electrodes.

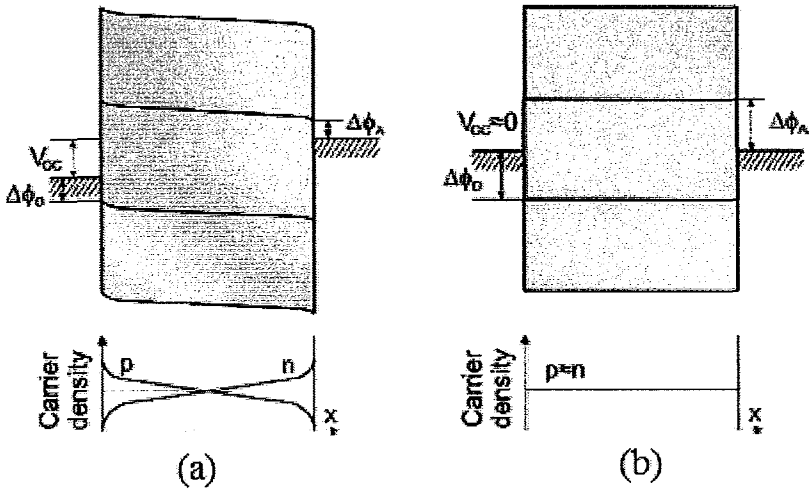

Figure 2-18 Schematic band diagrams and hole (p) and electron (n) carrier densities at open-circuit voltage (V_{OC}) conditions vs position (x) within the device for bulk heterojunctions.[61]

In a bulk heterojunction organic solar cell, the photogenerated carrier is distributed throughout the active layer. $\Delta\varphi$ of the difference between anode and cathode determines the built-in field that is associated with V_{OC} that also largely effects η_{cc}. The first case shown in Figure 2-18 (a), with small $\Delta\varphi$ or a built-in field, V_{OC} can lead to a maximum that is close to the difference between HOMO$_D$ and LUMO$_A$. For high $\Delta\varphi$ shown in Figure 2-18 (b), however, the built-in field is very low and limits the maximum

V_{OC}. Therefore, the anode and cathode materials should be optimized in order to get greater V_{OC}.

Another challenge for the bulk heterojunction solar cell is to achieve high η_{cc} by providing direct transport paths for the carriers to the electrodes. Hole and electron transport occurs via the separate donor and acceptor molecular networks. However, due to the large amounts of nearby D/A interface, carrier may have the possibility of recombination. An example is for the optimized blends of MDMO-PPV/PCBM and P3HT/PCBM, which shows simultaneously high I_{SC} and FF. However, these two devices suffer a big difference of the power conversion efficiency with 1.5% and 4.1%, respectively. For small molecule bulk heterojunction solar cells, there is a tendency to form uniformly mixed blends without significant phase separation that leads to low mobilities of holes, low η_{cc}, and high resistance. [86]

Therefore, the donor materials and acceptor materials can greatly reduce the cell efficiency not providing the necessary conductivity that carriers require in order to be collected in electrodes. In this view, ordered structures are supposed to improve conductivity of the system and thus cell efficiency. Another example is that in particular organic solar cells made of single-walled carbon nanotubes (SWNTs) as the acceptor and poly(3-octylthiophene) (P3OT) as the donor, the V_{OC} was found to be 0.75, much larger than expected. It was proposed that the improvement in the photovoltaic properties is caused by the internal polymer/nanotube links within the polymer matrix.[87]

Inorganic nanoparticles or nanorods can participate in the process as the acceptor material. In principle, polymer/nanoparticle hybrid solar cells should perform better than polymer/fullerene systems due to the additional higher absorption coefficient of inorganic semiconductor nanoparticles and higher intrinsic electron mobility compared to PCBM which is $10^{-3}cm^2V^{-1}s^{-1}$.[88] However, no higher power conversion efficiency η has been reported in hybrid solar cells compared to fullerene based organic solar cells so far. An important reason is that although the intrinsic conductivity within the individual nanocrystals is comparably high, the electron mobility in the nanocrystal network is quite low, which could be attributed to mainly the electrical insulating organic ligands on the nanocrystal surface.[89] In most cases, the ligands used for preventing aggregation of the nanocrystals contain long alkyl chains, which form electrically insulating layers and impede an efficient charge transfer between nanocrystals and polymer, as well as electron transport between the nanocrystals themselves. For example, a very low electron mobility of $10^{-5}cm^2V^{-1}s^{-1}$ was measured for CdSe covered with trioctylphosphine oxide (TOPO).[90] Extensive investigations on the surface modification of nanoparticles have been reported based on ligand exchange approaches by using various shorter capping ligands in order to overcome this problem, The interparticle distance is expected to be reduced, thus facilitating the electron transport through the nanoparticle domain phases. Furthermore, the solvent type, the hybrid compositions, film thickness, and process conditions should be carefully optimized to acquire large efficiency for conjugated polymer based hybrid solar cells.[72]

Above all, today's best bulk heterojunction solar cells are optimized in terms of η_{ED} and η_{CT}. The other steps in the conversion of photons to photocurrent still can be improved, such as the absorption efficiency η_A. Furthermore, it is quite clear that new materials have a key role to play in such processes.

2.5 Methods for fabrication of the active layer

Generally, the manufacturing processes of traditional inorganic solar cell have significantly high production and energy consumption since elevated temperature, high vacuum and numerous lithographic steps are involved. On the other hand, solar cells based on organic materials such as small molecules and conjugated polymers are able to be manufactured by low-temperature process.

2.5.1 Casting

Casting is probably the simplest film-forming technique available. No equipment is needed for this technique. The procedure is to simply cast a solution onto a substrate followed by drying. Though it is possible to prepare films of good quality, casting lacks control over the film thickness and film defects might be observed near the edge. Also there is a requirement that the material to be coated have a high solubility in the solvent and the precipitation be avoided.

2.5.2 Spin coating

The film-forming technique that indisputably has been most important for the development of polymer solar cells to this day is spin coating. It has several advantages over other coating techniques during drying which allows for the formation of very homogenous films over a large area. The typical spin coating process includes application of a liquid to a substrate followed by spinning at a chosen rotational acceleration speed of the substrate. Through spin coating, the thickness and morphology of the final film from a given solution at a certain concentration is highly reproducible. The advantage of spin coating is that parameters related to the ink and the interaction between the ink and the surface that is to be coated are not critical. However, several facts may limit the applicability for large area production. First, it requires the substrates to be handled individually. Second, the technique does not allow for patterning the formed film and this is expected to be crucial to the successful application of the technology. [91]

2.5.3 Electrodeposition

Electrodeposition is increasingly being used for the preparation of thin films and coatings since it has several advantages such as high purity of deposited materials, high deposition rate, good control over film properties and the possibility to deposit uniform coatings on substrates of complex shape and can be applied for quite a large range of different materials.[92] Electrodeposition can be performed by anodic or cathodic methods but the former has limited materials and substrates that can be used for deposition. It is thus that most materials used in thin-film solar cells are deposited through the cathodic method. Two processes are commonly used to prepare ceramic coatings by cathodic electrodeposition: the electrophoretic process (EPD), which is based on the use of suspensions of ceramic particles or polyelectrolytes, and the electrolytic process (ELD), which starts from solutions of metal salts.

EPD of polymers is achieved via the motion of charged polymer macromolecules in solution towards an electrode, and film formation under the influence of an electric field. It should be noted that although electrostatic repulsion can stabilize polymers in solution, it impedes film formation at the electrode surface.[93] Charged polymers can be categorized into two groups: strong polyelectrolytes, for which the degree of ionization is independent of the solution pH, and weak polyelectrolytes, for which the degree of ionization is determined by the solution pH. Recent studies have highlighted the advantages of weak polyelectrolytes for application in EPD[93]. It was shown that increased pH at the cathode surface promoted the charge neutralization of weak cationic polyelectrolytes, effectively precipitating the polymers at the cathode surface, resulting in film formation.[93] Conversely, decreased pH at the anode surface enable the charge neutralization of weak anionic polyelectrolytes and their deposition on the anode.[94] Cathodic EPD offers important advantages compared to the anodic method, as problems related to anodic oxidation and dissolution of metallic substrates can be avoided. Moreover, cathodic EPD of polymers can be combined with cathodic electrosynthesis of metals and oxides for the fabrication of nanocomposite films that form hybrid solar cells.

2.5.4 Roll-to-roll techniques

Roll-to-roll technique is the process of creating electronic devices on a roll of flexible plastic or metal foil that is in the form of a very long sheet wound on a roll and it has now been used for the fabrication of the polymer solar cells as an emerging technique. The substrate material in this case is often referred to as the web and it is required to have some mechanical flexibility. During printing and coating the web material is unwound from the roll and passed through the printing or coating machine and once through the process the material is rewound on a roll. For a polymer solar cell that comprises three printed or coated layers the distinction can be seen in Figure 2-19. There are a lot of practicalities that might associate with the machine such as tension and speed control of the web, cleaning of the web, removal of static electricity, surface treatments, IR-heating, hot-air drying, UV-treatment and web cooling. However, the process can hardly give a final film with a complex function, as it relies on the nanoscale morphology, molecular organization and interfaces between layers in multi- layer composite films.[91]

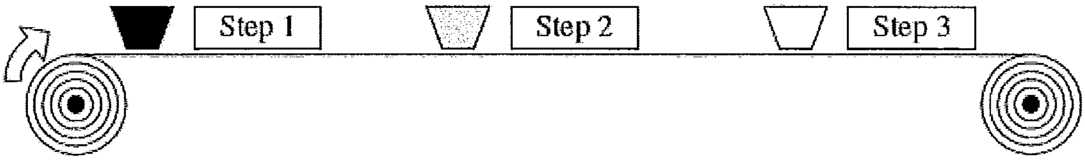

Figure 2-19 Illustration of roll-to-roll processing of a 3-layer polymer solar cell in an integrated process.[91]

3 Objectives

- Development of composite materials for applications in photovoltaic devices including organic solar cells and hybrid solar cells.
- Development of new methods for the fabrication of polymer-SWNTs and polymer-metal oxide nanocomposites.
- Development of electrophoretic methods for the deposition of poly[3-(3-N,N-diethylaminopropoxy)thiophene] (PDAOT) and co-deposition of PDAOT and poly(9,9-bis(diethylaminopropyl)fluorine-co-phenylene) (PDAFP).
- Development of new methods of dispersion and charging of ZnO and TiO_2 nanoparticles using new dispersing agents.
- Investigation of deposition mechanism, kinetics of deposition, deposition yield, film microstructure, composition and properties.

4 Experimental Procedures

4.1 Materials

4.1.1 Materials purchased from commercial suppliers

The materials listed in the

Table **4-1** were purchased from industrial suppliers and used for the fabrication of coatings by electrodeposition.

Table 4-1 Materials purchased from commercial suppliers

Material	Supplier	Purity and other specifications
Zinc oxide	Aldrich	<70nm
Titanium dioxide	Degussa	Anatase: rutile = 4:1, <25nm
Dopamine hydrochloride	Sigma	Reagent grade
Alizarin yellow	Aldrich	Dye content 50%
Titanium dioxide	Aldrich	Anatase, <25nm
Benzoic acid	Sigma-Aldrich	≥99.5%
4-hydroxybenzoic acid	Aldrich	≥99%
3,5-dihydroxybenzoic acid	Aldrich	97%
Gallic acid	Sigma	97.5-102.5% (titration)
Salicylic acid	Sigma-Aldrich	ACS reagent, ≥99.0%

Salicylic acid sodium salt	Sigma	≥99.5%
SWNTs	Carbon Nanotechnologies, Inc	Grade/Lot #: PO347
Acetic acid	Caledon Laboratories Ltd.	Reagent grade
Anhydrous Ethyl Alcohol	Commercial Alcohol Inc.	Reagent grade

4.1.2 Synthesis of PDAOT[95]

PDAOT was prepared by Prof. Alex Adronov's group from Department of Chemistry, McMaster University. The main steps of the synthesis method of PDAOT are illustrated in Figure 4-1.

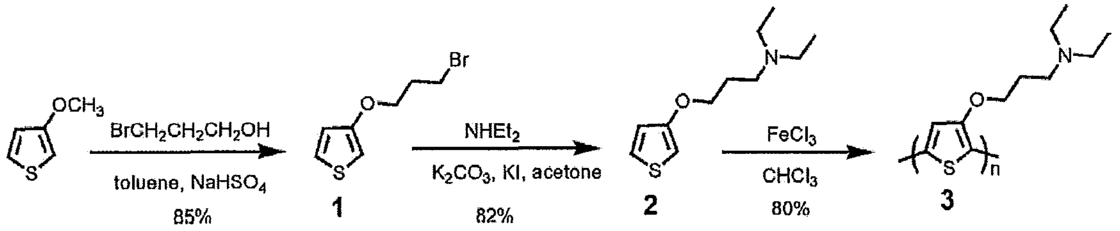

Figure 4-1 Synthesis of poly[3-(3-N,N-diethylaminopropoxy)thiophene] (PDAOT)[95]

4.2 Coating by electrodeposition methods

4.2.1 Experimental setup for electrodeposition

Both anodic and cathodic electrophoretic deposition method were employed in the fabrication of PDAOT-SWNTs, PDAOT-metal oxide nanoparticle composite coatings, and films of nanoparicles with dispersants. The electrodeposition cell included a substrate centered between two Pt counter electrodes. The distance between the substrate and counter electrodes was 15 mm. The volume of the cell was 300 ml. An electrophoresis power supply EPS 601 (Amersham Biosciences) was employed to provide the DC electric field for electrodeposition, either in a constant current density (galvanostatic) or a constant voltage mode.

4.2.2 Preparation of solutions and suspensions for electrodeposition

The neutral polymer PDAOT was protonated and dissolved in 0.2% acetic acid solution to the protonation of amine side chains, resulting in complete and rapid dissolution of the polymer in water or water-ethanol mixture (10%/90%), forming a purple solution of 6-9 g/L PDAOT.

Next different amounts of SWNTs or ZnO nanoparticles were added into the solution, and ultrasonicated for 2 hours to achieve a homogeneous dispersion. The concentration of SWNTs was between 0.06-0.6 g/L, while the concentration of ZnO was in the range of 0.5-4 g/L.

10 g/L ZnO suspension were prepared. Alizarin yellow were added into the suspension of which the concentration was between 0-0.4 g/L. Dopamine hydrochloride (DA) were added into 10 g/L ZnO suspension and the concentration of DA is between 0-0.05 g/L. Both of them were ultrasonicated for 2 hours. Electrodeposition was performed in pure ethanol.

10 g/L TiO_2 suspension was prepared. Different dispersants were used to form suspensions of which the concentrations of dispersants were in the range of 0-1 g/L. The dispersants included benzoic aicd, 4-hydroxybenzoic acid, 3,5-dihydroxybenzoic acid,

gallic acid, salicylic aicd, and salicylic acid sodium salt. Electrodeposition was performed in pure ethanol after ultrasonication for 2 hours.

4.2.3 Electrodeposition procedures

Cathodic and anodic deposits were obtained on various conductive substrates under constant current or constant voltage conditions. These substrates include stainless steel 304 foils (50×50×0.1 mm), Nitinol wires (0.4 mm diameter), Pt foils (50×50×0.1 mm) and platinized silicon wafers (10×50×1.5 mm).

The deposition time was varied in the range of 0-8 min to obtain deposits with different thicknesses. The coatings obtained were dried in air at room temperature. Multilayer coatings were prepared by alternate deposition from different solutions without waiting between deposition of individual layers.

4.3 Characterization of the coatings

4.3.1 Investigation of deposition yield

The electrodeposition yield was studied by weighing the deposited coating. A Mettler Toledo AX105 DeltaRange analytical balance, which has a readability of 0.01 mg, was used to measure the weight of the foil substrate before and after the deposition, followed by drying at room temperature for 24 hr. Then the weight of a deposited coating was obtained.

4.3.2 X-ray diffraction analysis

X–ray diffractometry (XRD) was used to determine the phase content in minerals and materials. In this work, a diffractometer (Nicolet 12) with monochromatized Cu Kα radiation at a scanning speed of 1°/min was used to determine the crystallinity and phase content of powders and coatings.

4.3.3 Thermogravimetric and differential thermal analysis

Thermogravimetric analysis (TGA) is an analytical technique used to determine a material's thermal stability and fraction of volatile components by monitoring the weight change that occurs as a specimen is heated. In addition to weight changes, the instruments also record the temperature difference between the specimen and one or more reference pans (differential thermal analysis, DTA), which can be used to monitor the energy released or absorbed via chemical reactions or phase transformations during the heating process.

In this work, the deposits removed from Pt substrates were studied by TGA and DTA, carried out in air at a heating rate of 5°C/min using a thermoanalyzer (Netzsch STA–409).

4.3.4 Scanning electron microscopy

The scanning electron microscope (SEM) is a type of electron microscope that images the sample surface by scanning it with a high-energy beam of electrons in a scan pattern. The electrons interact with the atoms that make up the image producing signals that contain information about the sample's surface topography, composition and other properties.

The microstructures of the deposited films were investigated by SEM using a JEOL JSM-7000F scanning electron microscope. The samples for SEM observations of film surfaces and cross sections were obtained by EPD of polymer and composite films on platinized silicon wafers. The samples were placed on a conductive sample holder using a conductive adhesive copper tape.

4.3.5 Fourier transform infrared spectroscopy

Fourier Transform Infrared Spectroscopy (FTIR) is an analytical technique used to identify organic (and in some cases inorganic) materials. This technique measures the absorption of various infrared light wavelengths by the material of interest. These infrared absorption bands identify specific molecular components and structures.

In this work, the deposits removed from Pt substrates were studied by FTIR using Bio-Rad FTS-40 instrument.

4.3.6 Ultraviolet–visible spectroscopy

Ultraviolet–visible spectroscopy refers to absorption spectroscopy in the ultraviolet-visible spectral region. The absorption in the visible range directly affects the perceived color of the chemicals involved. In this region of the electromagnetic spectrum, molecules undergo electronic transitions.

In this work, UV–vis spectra were measured by using a Cary 50 UV–vis spectrophotometer. The solution applied for Uv-vis spectroscopy was taken from films deposited on ITO (indium-tin oxide) substrates. These films were dissolved in ethanol-water mixture (v/v 90/10) containing 0.2% acetic acid and then ultrasonicated for 1 hour.

5 Experimental Results and Discussion

5.1 Electrodeposition of ZnO and composite films

5.1.1 Electrodeposition of ZnO and DA composite films

Cathodic deposits were obtained from 0.5–10 g/L ZnO suspensions in ethanol. However, the deposits obtained from such suspensions were agglomerated and non-uniform. In contrast, relatively uniform deposits were obtained from well-dispersed and stable suspensions of ZnO-containing dopamine hydrochloride (DA). The suspensions, prepared using DA as a dispersant, were stable at least 1 week after ultrasonic agitation. The structure of dopamine hydrochloride (DA) is shown in Figure 5-1a.

It is known that colloidal particles in suspensions exhibit a charge, which can be modified by the use of additives. The formation of cathodic deposits indicated that ZnO particles were positively charged in ethanol suspensions. Damodaran and Moudgil [96] have proposed a mechanism of particle charging, in which the adsorbed alcohol ionized into a protonated alcohol and an alkoxide ion, followed by the dissociation of the protonated alcohol. Pure alcohols can ionize in the following way:[96]

$$RCH_2OH + RCH_2OH \rightarrow RCH_2O^- + RCH_2OH_2^+ \qquad (5\text{-}1)$$

The dissociated alcohol and alkoxide ion desorbed into the solution, leaving a proton on the particle surface. This resulted in the formation of positively charged particles in the suspensions. It is suggested that the addition of DA to the suspensions resulted in the DA adsorption on the surfaces of ZnO particles. As a member of the catecholamine family, DA is a strong surface complexant, which bonds strongly to oxide surfaces (Figure 5-1b). [71, 97-99]

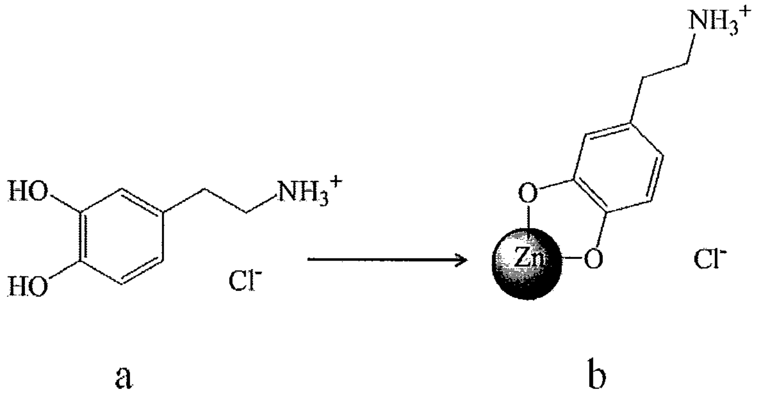

Figure 5-1 (a) Structure of dopamine hydrochloride (DA), (b) adsorption of protonated DA on the surface of zinc oxide (ZnO) particle.

5.1.1.1 Deposition yield study of ZnO and DA composite films

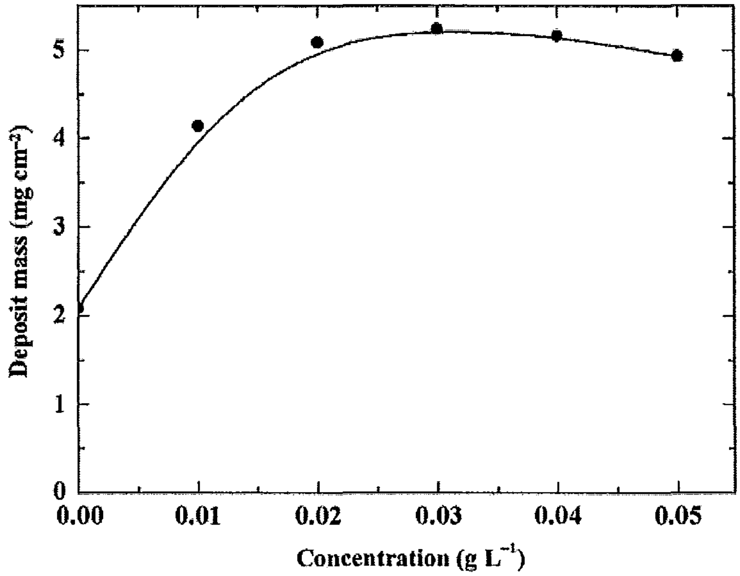

Figure 5-2 Deposit mass versus dopamine hydrochloride concentration for 10 g/L zinc oxide suspension at a deposition voltage of 20 V and a deposition time of 2 min.

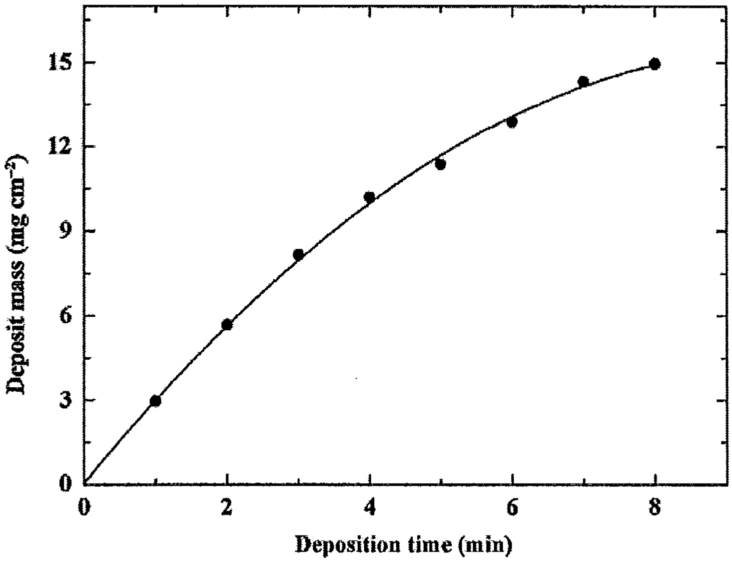

Figure 5-3 Deposit mass versus deposition time for 10 g/L zinc oxide suspension, containing 0.04 g/L dopamine hydrochloride at a deposition voltage of 20 V.

The addition of DA to the ZnO suspensions resulted in an increased deposition yield (Figure 5-2) in the DA concentration range of 0–0.02 g/L. Further increase in the DA concentration did not result in significant changes in the deposition yield. It is suggested that the adsorption of cationic DA (Figure 5-1) provided increased the charge of the ZnO particles and increased the deposition rate (Figure 5-2). The deposit mass increased with increasing deposition time (Figure 5-3). The increase in the deposit mass indicated that the deposition yield can be varied. However, the deposition rate decreased with time. The decrease in the deposition rate with time was observed in other investigations [100] and was attributed to the decrease in the voltage drop in the suspension and the increase in the voltage drop in the deposited layer.

5.1.1.2 FTIR study of ZnO and DA composite films

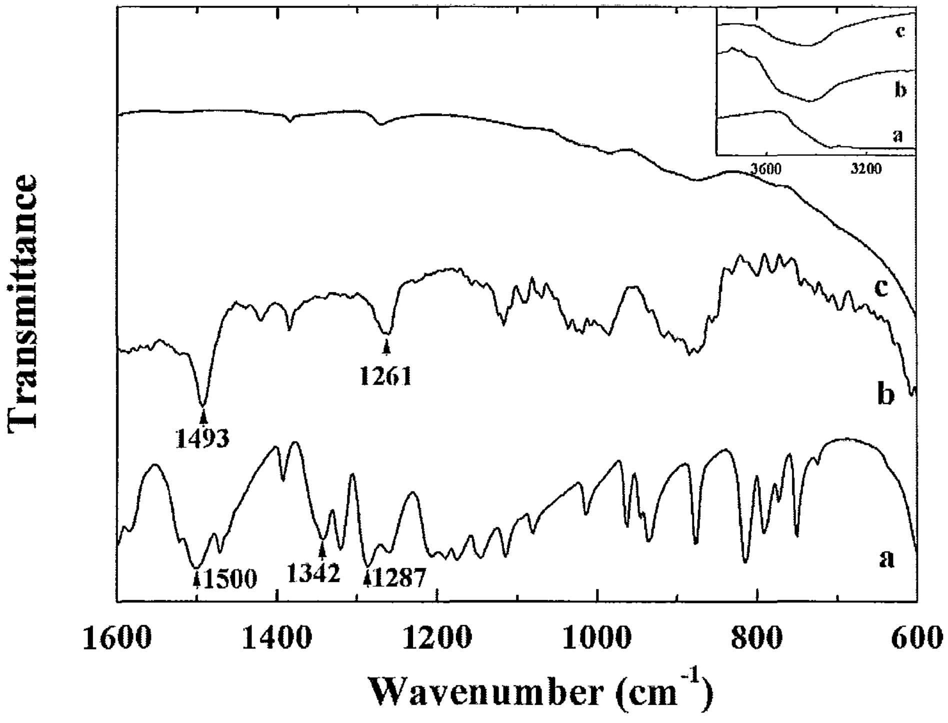

Figure 5-4 Fourier-transform infrared spectra of (a) as-received dopamine hydrochloride (DA), (b) deposit obtained from the 10 g/L ZnO suspension containing 0.04 g/L DA, (c) as-received zinc oxide (ZnO)

Figure 5-4a–c compare FTIR spectra of the as-received ZnO powder, DA, and the deposit prepared from the ZnO suspension in ethanol, containing DA. The FTIR spectrum of the commercial ZnO powder (Figure 5-4c) showed small peaks at 1629, 1384, and 1270 cm^{-1}, which can be attributed to the adsorbed CO_2.[101, 102] The FTIR spectrum of the deposit (Figure 5-4b) showed additional peaks, related to the adsorbed DA. The adsorption at 1493 cm^{-1} is due to the bending vibration of C–H groups of DA. The bands at 1248 and 1101 cm^{-1} can be attributed to the aryl-oxygen stretching vibrations.[97, 103] However, the adsorption related to the bending vibrations of DA OH [98] groups at 1342 cm^{-1} was not observed. This is in a good agreement with the mechanism of DA adsorption on oxide particles, which involves chelation (Figure 5-1b) of surface metal ions.24, [98, 104]

5.1.1.3 SEM study of ZnO and DA composite films

Figure 5-5 SEM images of zinc oxide (ZnO) film prepared from 10 g/L ZnO suspension, containing 0.04 g/L dopamine hydrochloride (DA) at a deposition voltage of 20 V.

Figure 5-5 shows SEM images of films deposited by cathodic deposition. The deposition resulted in the formation of porous films. The porosity can be attributed to gas evolution at the electrode surface. According to the data provided by the manufacturer, the average particle size of the ZnO powder was 70 nm. The SEM image of the deposit showed a large number of particles with particle size below 70 nm. However, the deposit also included larger particles with particle size of 100–200 nm. The film thickness varied in the range of 1–20 mm by variation in the deposition time and voltage.

5.1.2 Co-deposition of $ZnO-TiO_2$ DA composite films

Previous investigations showed that composite ceramic materials can be deposited by EPD using similar charging additives for individual components.[93, 105, 106] It is suggested DA can be used for the EPD of other oxides and the fabrication of composite materials. As a step in this direction, the deposition of TiO_2 films from the solutions containing DA has been investigated. The mechanism of DA adsorption on the surface of TiO_2 powders was investigated in the literature.[71, 97] It was shown that DA adsorption involves the complexation of Ti^{4+} ions. This mechanism is similar to the mechanism of DA adsorption on ZnO particles.

5.1.2.1 SEM study of $ZnO-TiO_2$ DA composite films

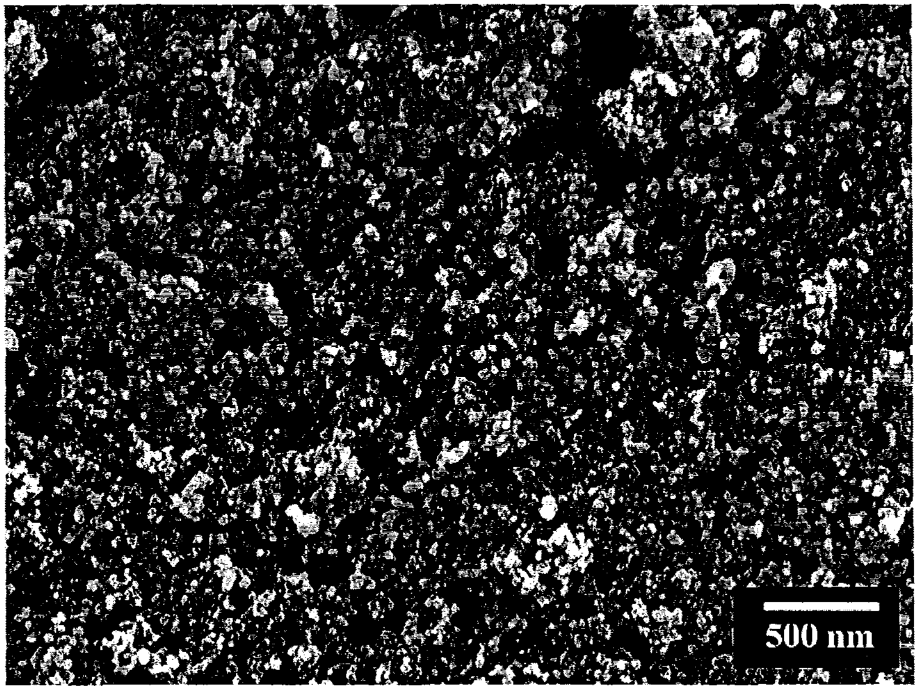

Figure 5-6 SEM images of TiO_2 film prepared from 10 g/L TiO_2 suspension, containing 0.04 g/L DA at a deposition voltage of 20 V.

Figure 5-6 shows the SEM image of the film prepared by cathodic EPD from the TiO_2 suspension containing DA. The size of the deposited TiO_2 particles is about ~30 nm, in agreement with the data provided by the manufacturer. However, SEM investigations of as received powders showed that some primary nanoparticles formed agglomerates, which were also observed in the deposited films. The addition of ZnO to the TiO_2 suspensions resulted in the codeposition of TiO_2 and ZnO. The SEM image of the composite films showed small TiO_2 particles and larger ZnO particles.

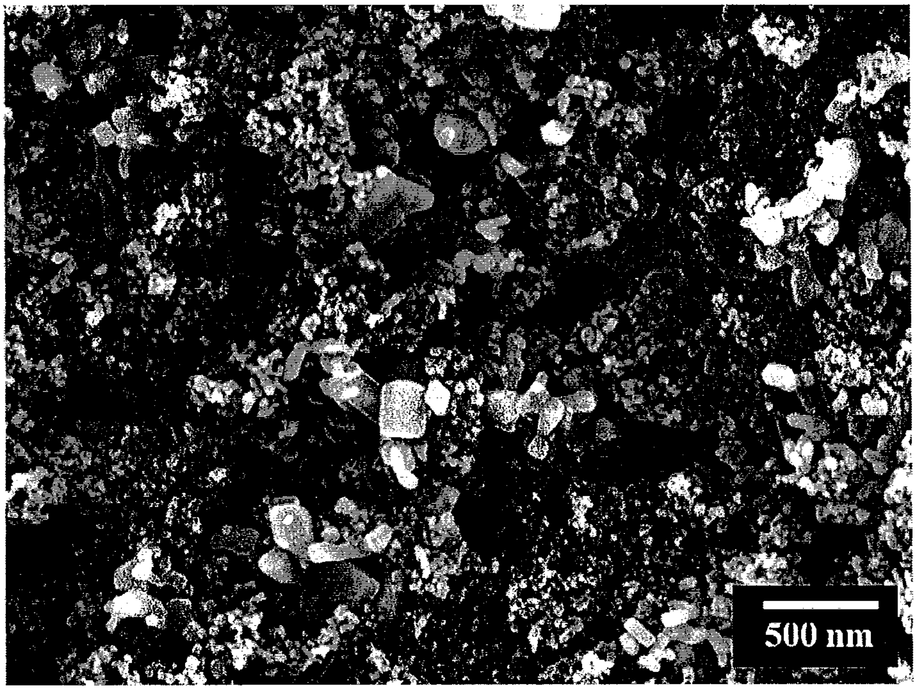

Figure 5-7 SEM images of composite TiO_2–ZnO film prepared from a suspension containing 10 g/L TiO_2, 4 g/L ZnO, and 0.04 g/L DA at a deposition voltage of 20 V.

5.1.2.2 XRD study of ZnO–TiO_2 DA composite films

XRD studies (Figure 5-8) of the composite films showed peaks of TiO_2 (anatase and rutile) and ZnO in agreement with the corresponding JCPDS files. Therefore, the results of SEM and XRD studies showed codeposition of ZnO and TiO_2 nanoparticles and the formation of composite films. These results are in good agreement with EDS data.

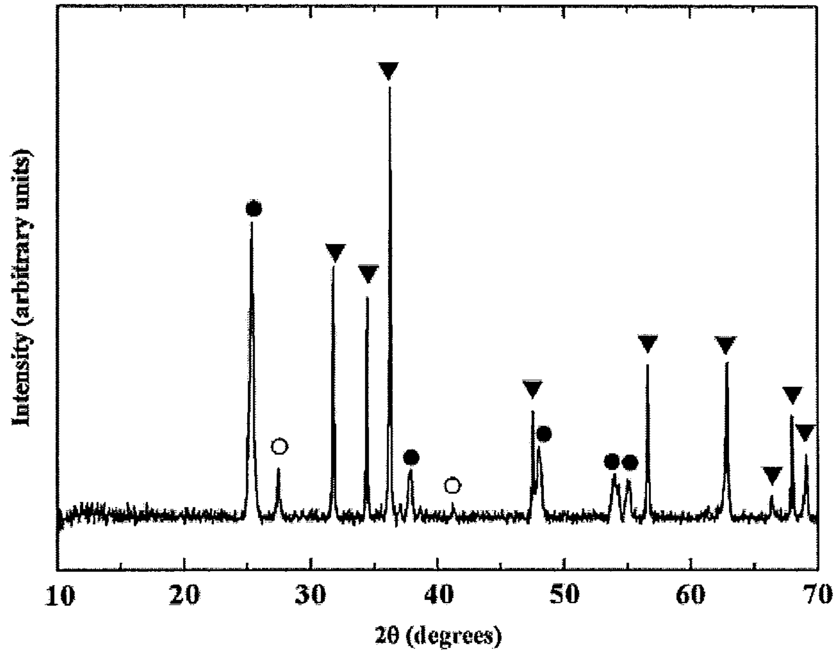

Figure 5-8 X-ray diffraction pattern of a composite TiO_2–ZnO film prepared from the suspension containing 10 g/L TiO_2, 4 g/L ZnO, and 0.04 g/L dopamine hydrochloride (DA) at a deposition voltage of 20 V (•, TiO_2 anatase, JCPDS file 21-1272; ○, TiO_2 rutile, JCPDS file 21-1276; ▼, ZnO, JCPDS file 36-1451).

5.1.3 Electrodeposition of ZnO and alizarin yellow composite films

The addition of Alizarin Yellow (AY) (Figure 5-9a) to the ZnO suspension resulted in the formation of anodic deposits. (Figure 5-9b)

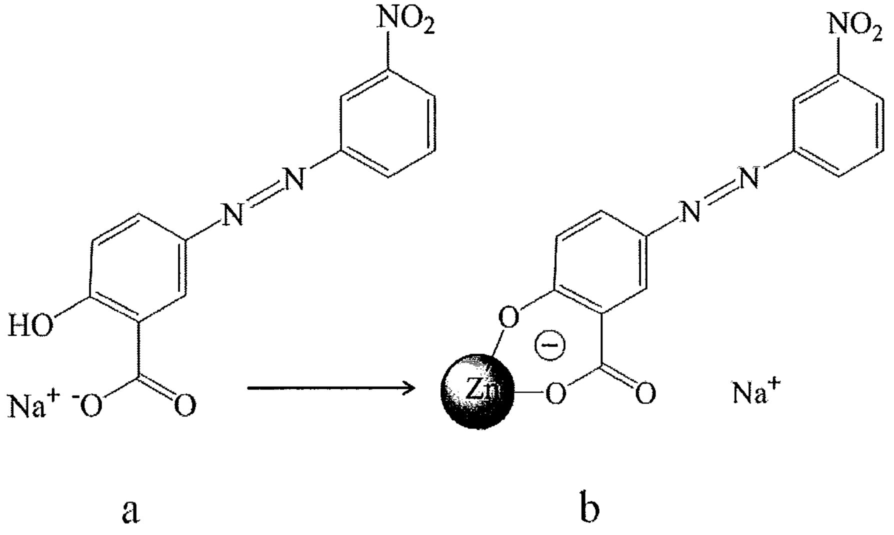

Figure 5-9 (a) Structure of alizarin yellow (AY), (b) adsorption of AY on the surface of zinc oxide (ZnO) particle.

5.1.3.1 Deposition yield study of ZnO and AY composite films

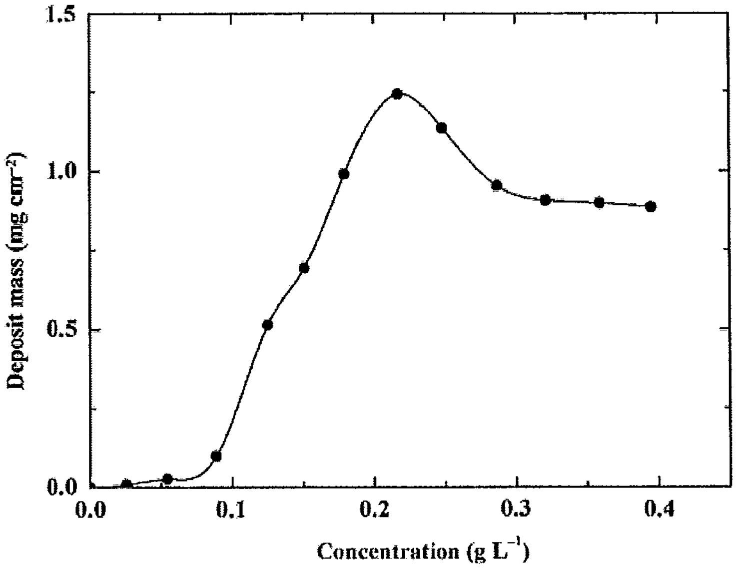

Figure 5-10 Deposit mass versus alizarin yellow concentration in 10 g/L zinc oxide suspensions at a deposition voltage of 20 V and a deposition time of 1 min.

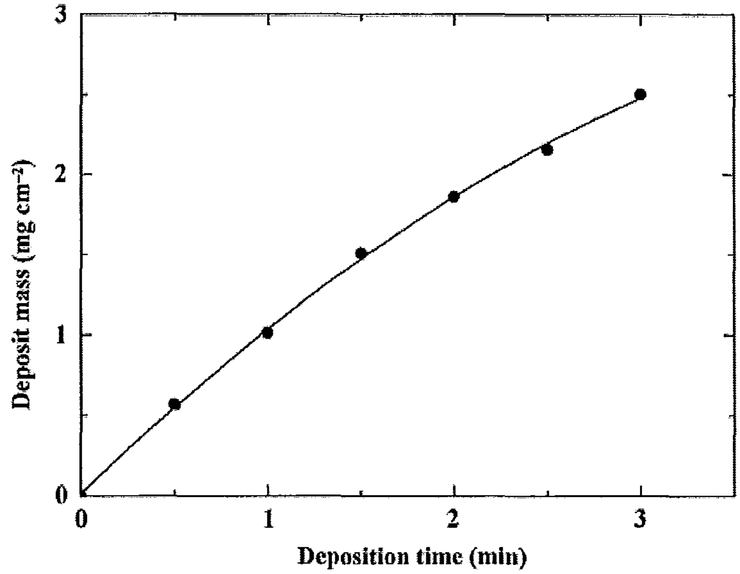

Figure 5-11 Deposit mass versus deposition time for 10 g/L zinc oxide suspension, containing 0.4 g/L alizarin yellow at a deposition voltage of 20 V.

Figure 5-10 shows deposit mass versus AY concentration in the ZnO suspensions. As pointed out above, ZnO particles were positively charged in the ethanol suspension. The adsorption of AY on the surface of the ZnO particles resulted in a charge reversal. As a result, anodic deposits were obtained at AY concentrations above 0.025 g/L AY. Sedimentation experiments showed stability of the suspensions during 2–3 days. The deposition yield increased significantly with increasing AY concentration in the range from 0.09 to 0.21 g/L and decreased at higher concentrations. It should be noted that the increase in AY concentration above ~0.2 g/L resulted in a lower suspension stability attributed to the increased ionic strength. As a result, the concentration dependence of the deposition yield showed a maximum (Figure 5-10). The deposit mass increased with increasing deposition time (Figure 5-11). Therefore, the amount of the material deposited anodically can be varied.

5.1.3.2 FTIR study of ZnO and AY composite films

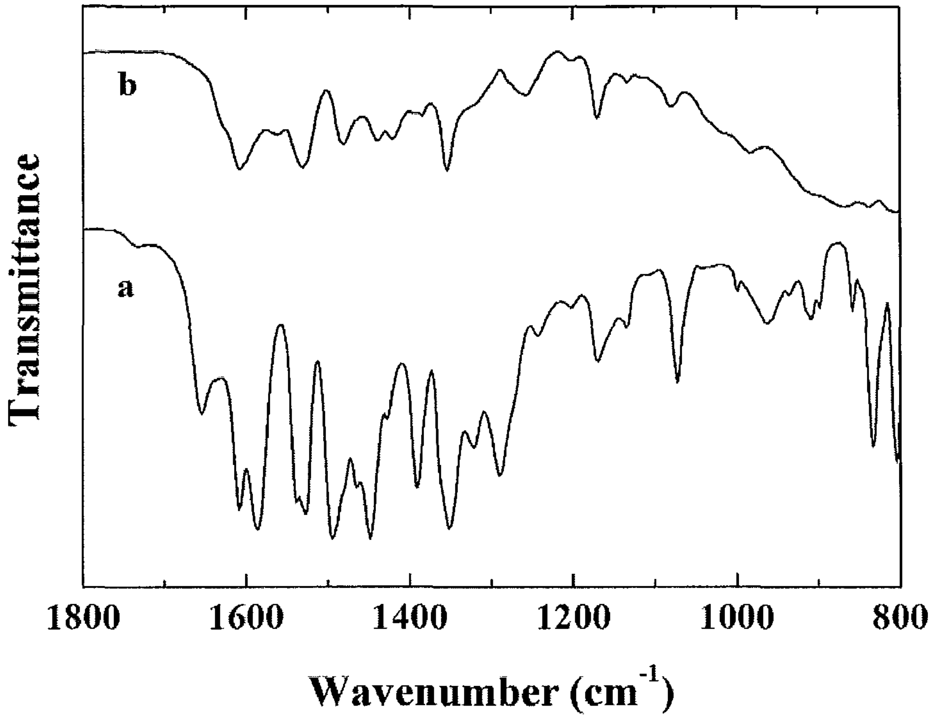

Figure 5-12 Fourier-transform infrared spectra of (a) as-received alizarin yellow (AY) dye, and (b) a deposit prepared from the 10 g/L ZnO suspension containing 0.4 g/L AY dye.

The comparison of the FTIR data for the as-received ZnO powder, AY powder, and the deposit obtained from the ZnO suspension containing AY (Figure 5-4c, Figure Figure 5-12a and b) showed that AY was adsorbed on the surface of ZnO particles. The FTIR spectrum of the deposit (Figure 5-12b) showed absorption peaks at 1607, 1481, and 1079 cm^{-1}, which can be attributed to the C=C ring stretching bands [107, 108] of the adsorbed AY. The as-received AY powder showed similar peaks (Figure 5-12a). The peak at 1350 cm^{-1} attributed to the stretching C=O vibrations of the carboxylic groups [108] in the spectrum of the AY (Figure 5-12a) shifted to 1354 cm^{-1} in the spectrum of the deposit (Figure 5-12b). The new band in the spectrum of the deposit at 1257 cm^{-1} was attributed to the aryl-oxygen stretching vibrations. [97, 103, 109] However, the adsorption related to the bending vibrations of phenolic OH groups was not observed in the spectrum of adsorbed AY. The strong band related to the asymmetric vibration of COO^- for the as received AY (Figure 5-12a) at 1586 cm^{-1} was not observed in the spectrum of the adsorbed AY (Figure 5-12b). This can be attributed to the formation of bridging complexes.[109, 110] Therefore, it is suggested that the mechanism of AY adsorption on the ZnO surface (Figure 5-9b) is similar to that proposed for the adsorption of salicylic acid, where substituent hydroxy groups are involved in carboxylate surface coordination.[109, 110]

5.1.3.3 SEM study of ZnO and AY composite films

Figure 5-13 shows an SEM image of the films deposited by anodic deposition. The deposition resulted in the formation of porous films. The porosity can be attributed to gas evolution at the electrode surface.

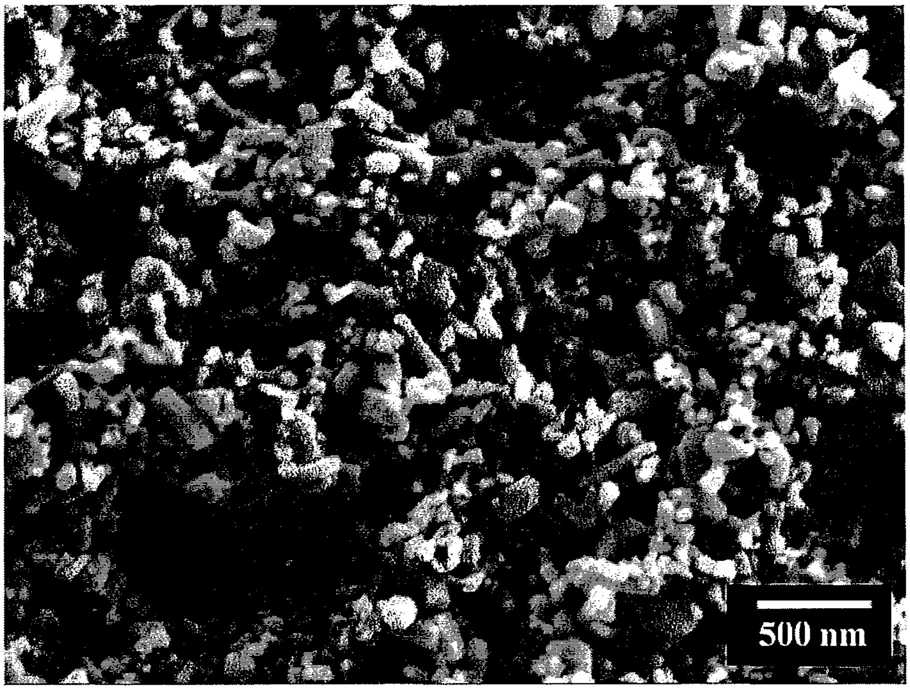

Figure 5-13 SEM images of ZnO film prepared from 10 g/L ZnO suspension, containing 0.4 g/L alizarin yellow (AY)

5.2 Electrodeposition of PDAOT and composite films

5.2.1 Electrodeposition of PDAOT

Cathodic deposits were obtained from 5 to 9 g L^{-1} PDAOT solutions in water and in a mixed ethanol/water solvent (90/10 v/v). It is suggested that the deposition mechanism is based on the electrophoretic motion of protonated PDAOT–H^+ towards the cathode, where the pH is high due to the reaction:

$$2H_2O + 2e^- \rightarrow H_2 + 2OH^- \qquad (5\text{-}2)$$

The charge neutralization of the PDAOT–H^+ in the high pH region at the cathode surface resulted in the PDAOT precipitation and the formation of insoluble films:

$$\text{PDAOT–H}^+ + OH^- \rightarrow \text{PDAOT} + H_2O \qquad (5\text{-}3)$$

It was found that pinhole-free films can be obtained from aqueous PDAOT solutions at low voltages in the range of 3–5 V. However, more uniform films of PDAOT were produced when an ethanol/water mixture (90/10 v/v) was used as the solvent, offering the advantage of reduced gas evolution from electrolysis of water. In the case of the ethanol/water solvent system, the deposition voltage was varied in the range of 5–15 V.

5.2.1.1 SEM studies of PDAOT films

Figure 5-14 shows typical SEM images of the cross section of the PDAOT film prepared by EPD. The deposition resulted in the formation of dense and uniform films. SEM studies showed that film thickness could be varied in the range of 0–5 μm by adjusting the deposition voltage (from 5 to 15 V) and deposition time (0–10 min). The increase in the film thickness with increasing voltage was attributed to increasing electric field in the suspension, which, in turn, increased the speed of electrophoretic motion of polymer macromolecules and resulted in higher deposition yield.[93, 105, 111]

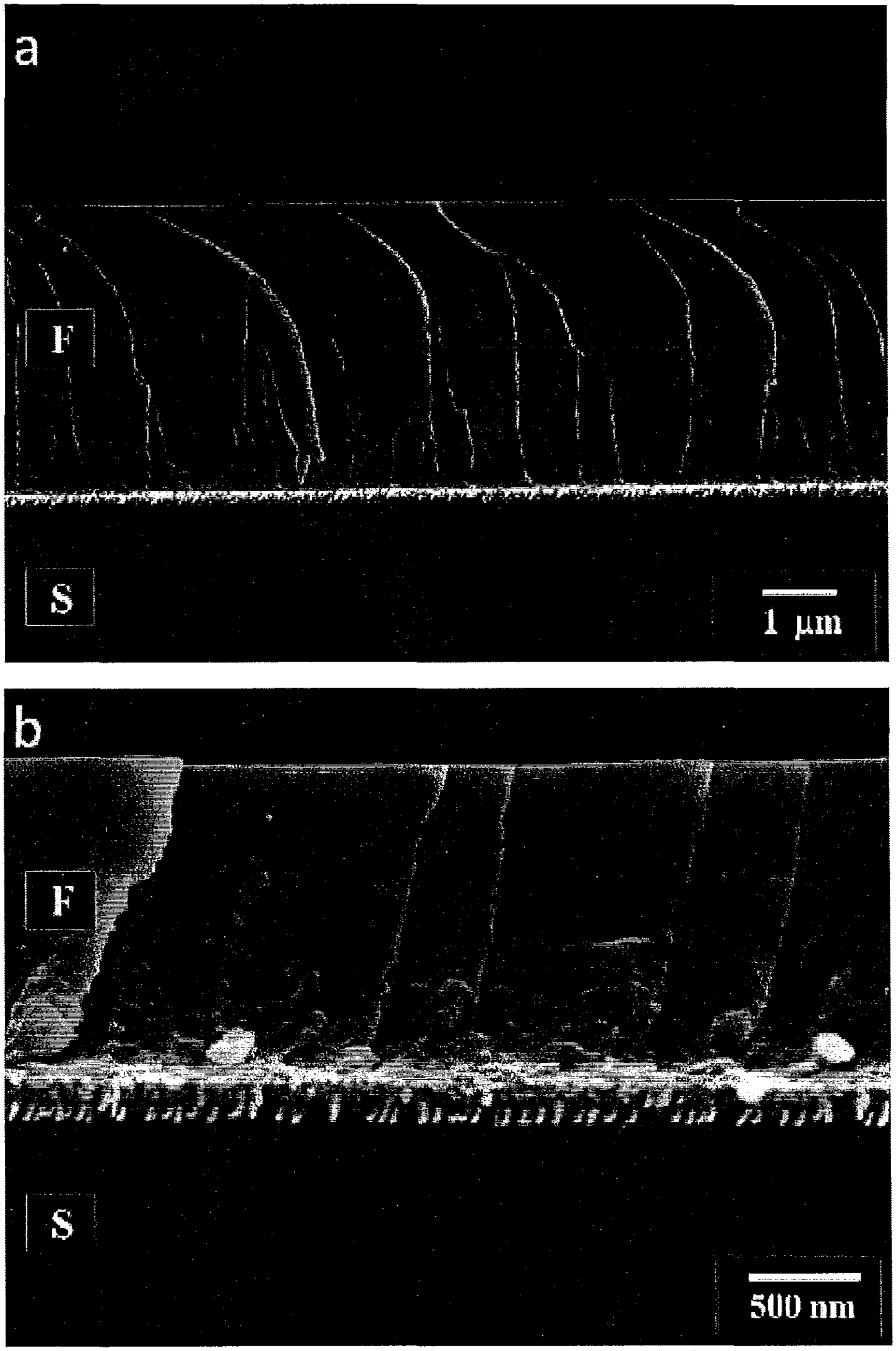

Figure 5-14 SEM images of PDAOT films deposited on the platinized silicon wafers: (a) from 6 g/L PDAOT solution in water at a deposition voltage of 4 V and (b) from 9 g/L PDAOT solution in a mixed ethanol–water solvent at a deposition voltage of 6 V (F:film, S:substrate).

5.2.2 Electrodeposition of composite PDAOT–SWNTs films

EPD has been employed for the fabrication of composite films containing SWNTs in a PDAOT matrix. However, the fabrication of composite films at low cell voltages from aqueous solutions presented difficulties. It should be noted that electric field is an important factor, controlling the deposit microstructure and deposition efficiency. It is known that more adherent and continuous coatings with less cracking can be obtained at lower electric fields.[105] However, a minimum electric field is necessary in order to overcome inter-particle interactions and to allow particles to bond to the substrate. [105] Composite films were obtained from the solutions in a mixed ethanol–water solvent system using higher voltages (up to 15 V) and, therefore, higher electric fields.

5.2.2.1 SEM studies of composite PDAOT–SWNTs films

Figure 5-15 shows SEM images of the films prepared from solutions of PDAOT–SWNT complexes in a mixed ethanol/water solvent system. The images show SWNTs distributed in the PDAOT matrix. Analysis of these SEM images indicated that increasing the concentration of SWNTs in solution resulted in increased SWNT incorporation within the films. As an example, Figure 5-15(b) shows a larger number of SWNTs compared to Figure 5-15(a), due to the higher concentration of SWNTs in the solution. The mechanism of film formation is based on the co-deposition of PDAOT and PDAOT–SWNT complexes, as both components are positively charged under acidic conditions and therefore will migrate towards and deposit on the cathode.

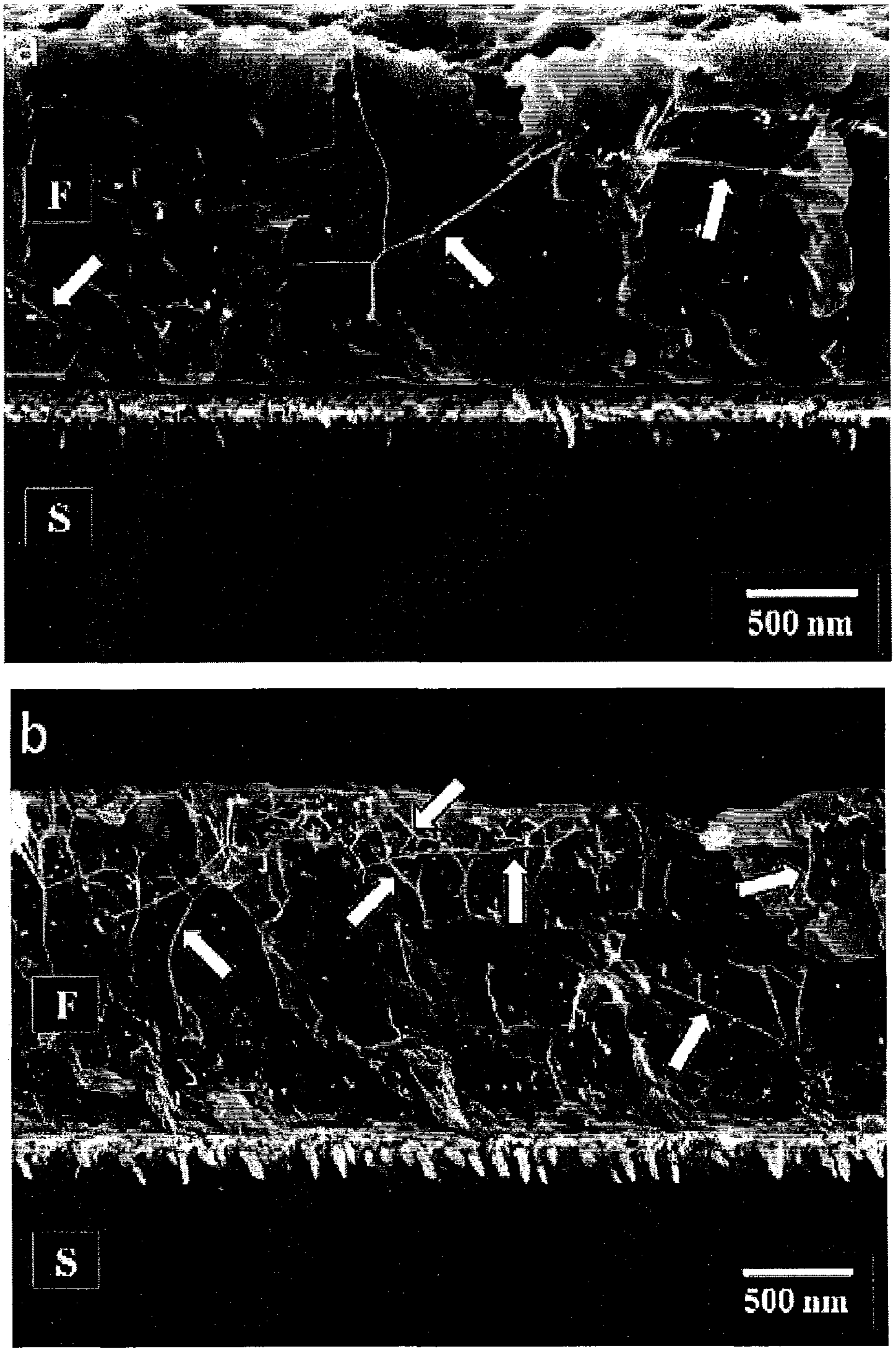

Figure 5-15 SEM images of cross sections of films prepared from (a) 9 g/L PDAOT solutions, containing 0.09 g/L SWNTs and (b) 9 g/L PDAOT solutions, containing 0.9 g/L SWNTs in a mixed ethanol–water solvent at the deposition voltage of 6V (F:film, S:substrate, arrows show SWNTs).

5.2.3 Co-deposition of composite PDAOT–PDAFP films

Since conjugated polymer has narrow absorption range compared with crystalline silicon, two kinds of polymers with different absorption spectrum were co-deposited in order to broaden the absorption range, and therefore increase the η_A.

5.2.3.1 Ultraviolet–visible spectroscopy study of composite PDAOT–PDAFP films

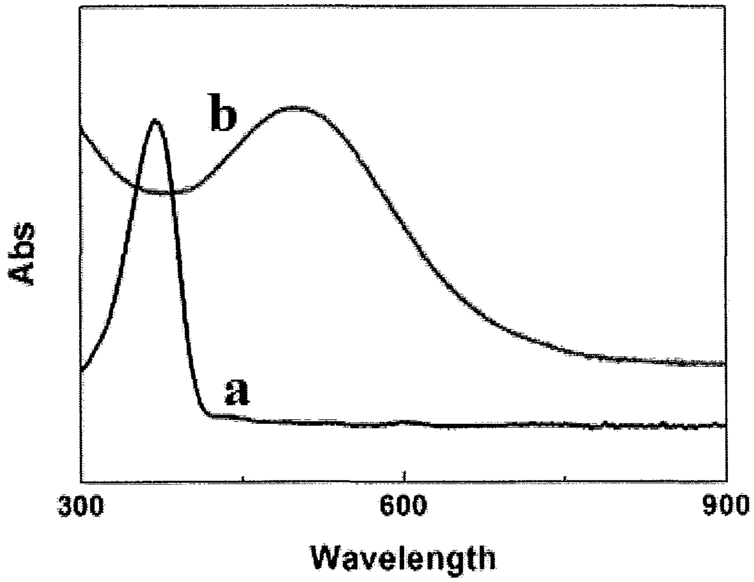

Figure 5-16 Uv–vis absorption data for (a) PDAFP, (b) PDAOT.

Figure 5-16 shows Uv-vis absorption spectrums of PDAFP (a) and PDAOT (b), respectively. PDAFP centered at 375 nm while PDAOT centered at 570 nm.

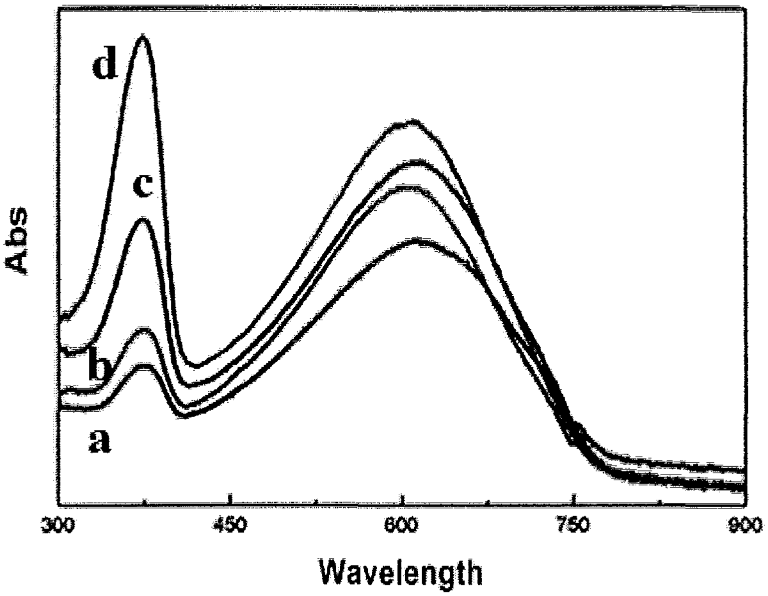

Figure 5-17 Uv–vis absorption data for (a) 5.58 g/L PDAOT with 7.5%PDAFP, (b) 5.46 g/L PDAOT containing 10%PDAFP, (c) 5 g/L PDAOT containing 20% PDAFP, (d) 4.29 g/L PDAOT containing 40%PDAFP.

Figure 5-17 shows the Uv-vis absorption spectrum was adjustable by controlling the amount of PDAFP in PDAOT solution.

5.2.4 Electrodeposition of composite PDAOT–ZnO films

The EPD method has also been employed for the fabrication of PDAOT–ZnO composite films from PDAOT solutions in a mixed ethanol/water solvent, containing ZnO nanoparticles. The process contains two steps: the motion of charged PDAOT and ZnO nanoparticles in a liquid toward an electrode under the influence of an electric field and the deprotonation and formation of a deposit of PDAOT–ZnO composites on the cathodic electrode.

5.2.4.1 XRD studies of composite PDAOT–ZnO films

The XRD studies of the films showed peaks corresponding to the JCPDS file 36-1451 of ZnO (Figure 5-18) and indicated the formation of composite PDAOT–ZnO films.

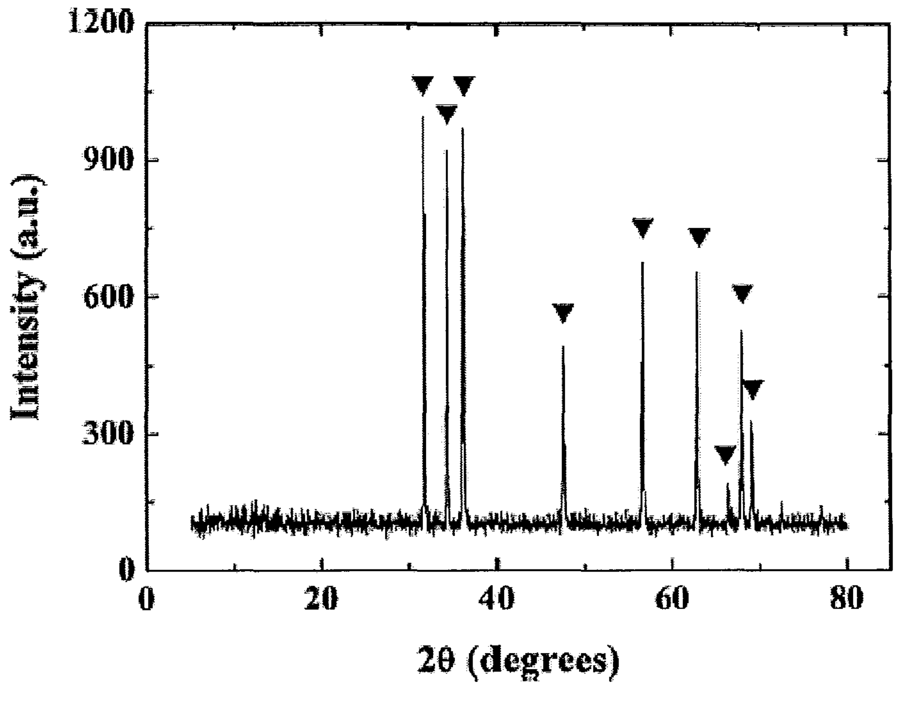

Figure 5-18 X-ray diffraction pattern of the deposit obtained from 6 g/L PDAOT solution, containing 4 g/L ZnO in a mixed ethanol–water solvent at the deposition voltage of 10V (▼ :peaks corresponding to JCPDS file 36-1451 of zinc oxide).

5.2.4.2 TGA&DTA studies of composite PDAOT–ZnO films

The ZnO content in the same films was estimated using TGA. Figure 5-19 compares the TGA (Figure 5-19a, b) and DTA (Figure 5-19c, d) data for the composite film and pure PDAOT. The TGA data (Figure 5-19a) for the pure PDAOT showed several steps in the mass loss below 600°C related to the thermal decomposition of the polymer.

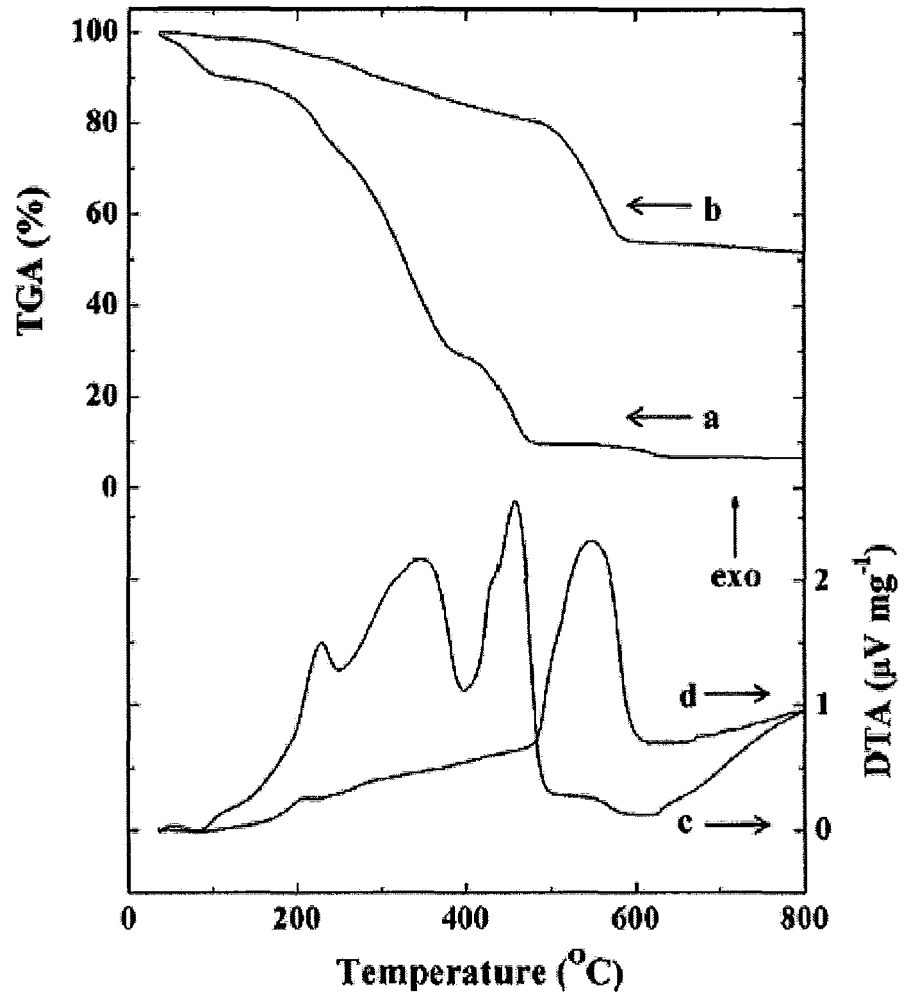

Figure 5-19 (a, b) TGA and (c, d) DTA data for (a, c) PDAOT powder and (b, d) deposit prepared from 6 g/L PDAOT solution, containing 4 g/L ZnO in a mixed ethanol–water solvent at the deposition voltage of 10 V.

The corresponding DTA data (Figure 5-19c) showed exotherms in the range of 200–600°C, related to the thermal decomposition of the polymer. The TGA (Figure 5-19b) data for the composite film showed continuous reduction in the sample mass in the range 20–500 C and an additional step in mass loss in the range of 500–600°C. The total mass loss at 800°C was found to be 48.2%. The mass loss can be attributed to film dehydration at lower temperatures and decomposition of the polymer side chains and backbone at higher temperatures. From the TGA data, the ZnO content in the sample was estimated to be ~51.8%. The corresponding DTA (Figure 5-19d) data showed a small exotherm in the range of 200–220°C and large exotherm in the range of 500–600°C, related to decomposition of the polymer. The TGA and DTA data showed that polymer decomposed at a higher temperature in the presence of ZnO. It should be noted that TGA and DTA studies were performed at a heating rate of 5°C min^{-1}. The ceramic phase can limit [112] the transport of O_2 and reaction products, resulting in a higher temperature of polymer burnout. The higher temperature of polymer burnout can also be attributed to polymer–ZnO interactions. It is in this regard that the complexation of amino groups of polymers with Zn ions [113] was found to enhance polymer thermal stability.

5.2.4.3 SEM studies of composite PDAOT–ZnO films

Figure 5-20 and Figure 5-21 show SEM images of the cross sections and surfaces of the films prepared from the PDAOT solutions containing ZnO. The SEM images indicated the formation of relatively dense films, containing ZnO particles in the PDAOT matrix. The films were relatively uniform (Figure 5-20) throughout a variety of film thicknesses, which were varied in the range of 0–10 μm. As in the case of SWNTs, increasing the ZnO concentration in solution resulted in an increased concentration of the ZnO particles in the deposit (Figure 5-21). The SEM images indicate that the size of the ZnO particles is in the range of 50–100 nm in agreement with the data provided by the manufacturer. However, some ZnO particles formed agglomerates, containing several particles.

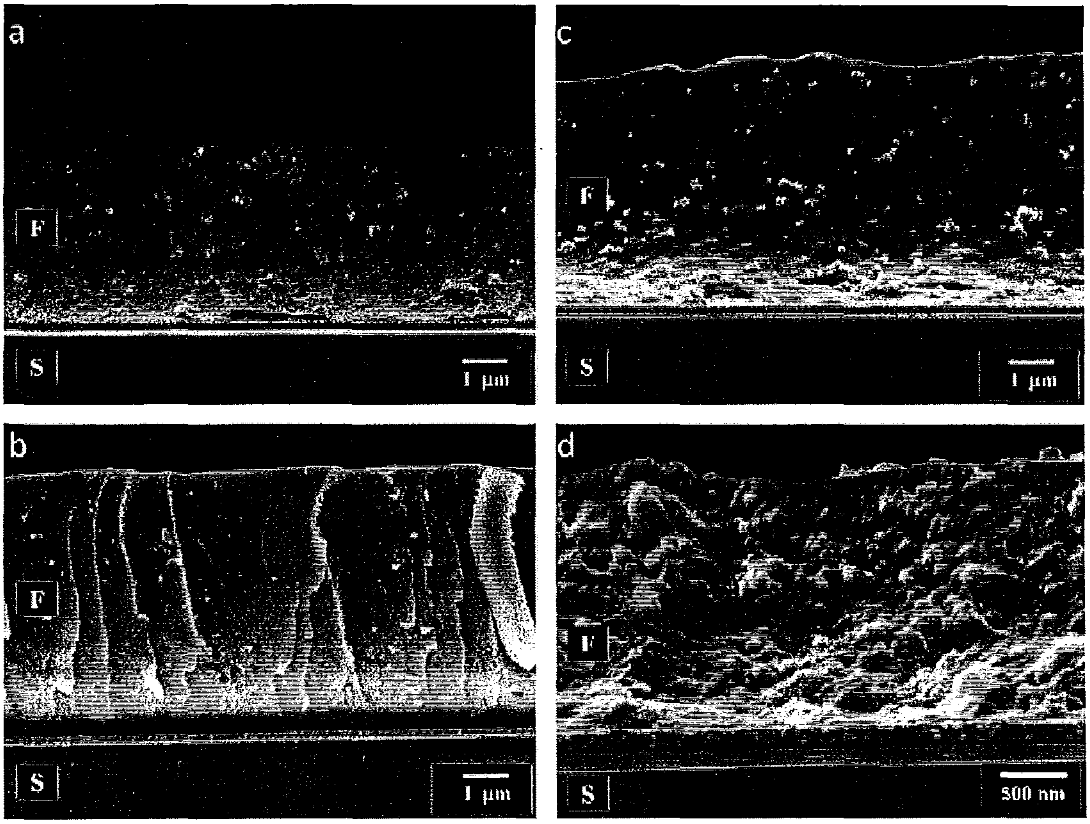

Figure 5-20 SEM images of the cross sections of the films deposited on the platinized silicon wafers from the 6 g/L PDAOT solutions, containing (a) 0.5 g/L, (b) 1.0 g/L, (c) 2.0g/L and (d) 4.0 g/L ZnO in a mixed ethanol–water solvent at the deposition voltage of 10V (F:film, S:substrate).

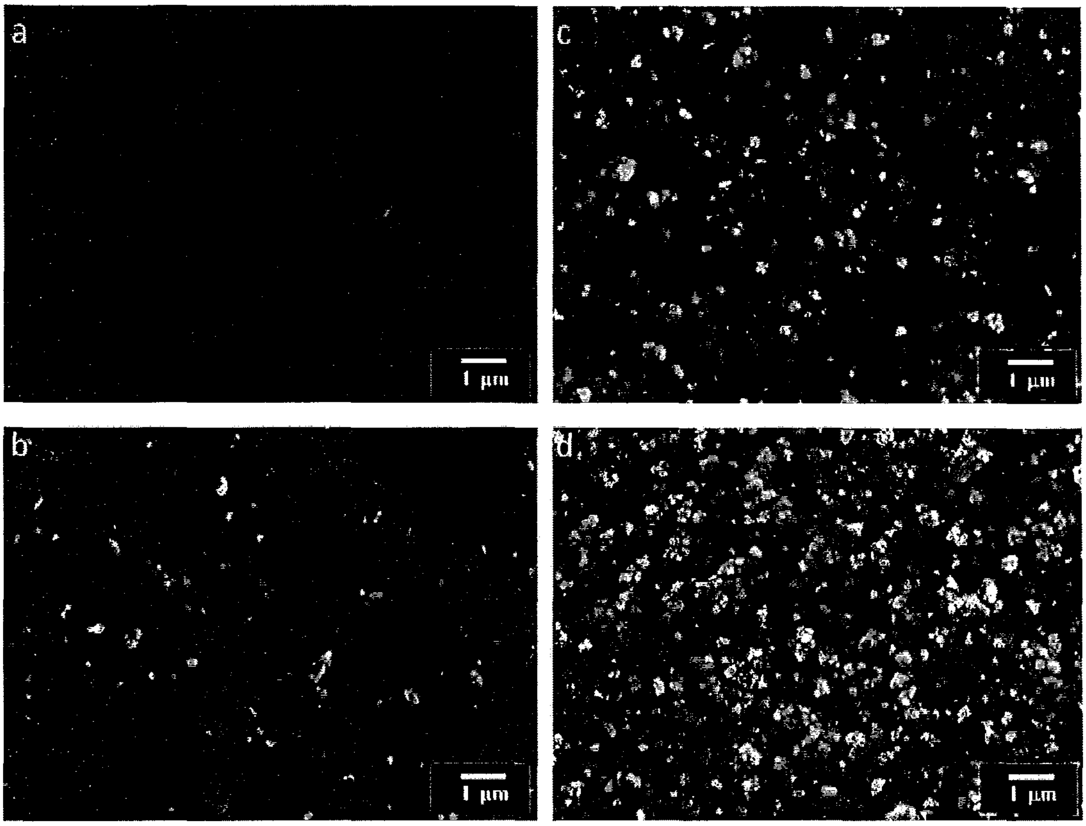

Figure 5-21 SEM images of the surfaces of the films deposited on the platinized silicon wafers from the 6 g/L PDAOT solutions, containing (a) 0.5 g/L, (b) 1.0 g/L, (c) 2.0 g/L and (d) 4.0 g/L ZnO in a mixed ethanol–water solvent at the deposition voltage of 10 V.

It is known from the literature [114] that the incorporation of small inorganic particles into a polymer matrix presents difficulties related to the tendency of particles to agglomerate. The agglomeration can result from van der Waals forces between particles or it can be attributed to the bridging flocculation of the particles, containing adsorbed polymer. It is known that the electric field present during EPD can promote the agglomeration of nanoparticles.[93, 111] The agglomeration of ZnO nanoparticles is especially evident from the SEM image obtained at lower magnification (Figure 5-22a) for the deposit obtained at a deposition voltage of 15 V. The SEM image shows non-uniform distribution of ZnO in the PDAOT matrix. The analysis of the SEM image revealed areas where agglomeration of ZnO particles occurred (Figure 5-22a, arrows), surrounded by areas where individual ZnO nanoparticles predominate.

5.2.4.4 SEM studies of composite PDAOT–ZnO–DA films

It was found that the dispersion of ZnO in the polymer matrix can be improved using protonated dopamine (DA). Figure 5-22b indicates that a more uniform distribution of ZnO particles with reduced particle agglomeration can be achieved using DA as a dispersant. Previous studies have shown that DA is capable of adsorption to the surface of ZnO and other oxides through ion complexation.[97, 98, 115, 116] In the present case, surface adsorption of protonated DA leads to electrostatic repulsion of nanoparticles, producing films with significantly decreased agglomeration.

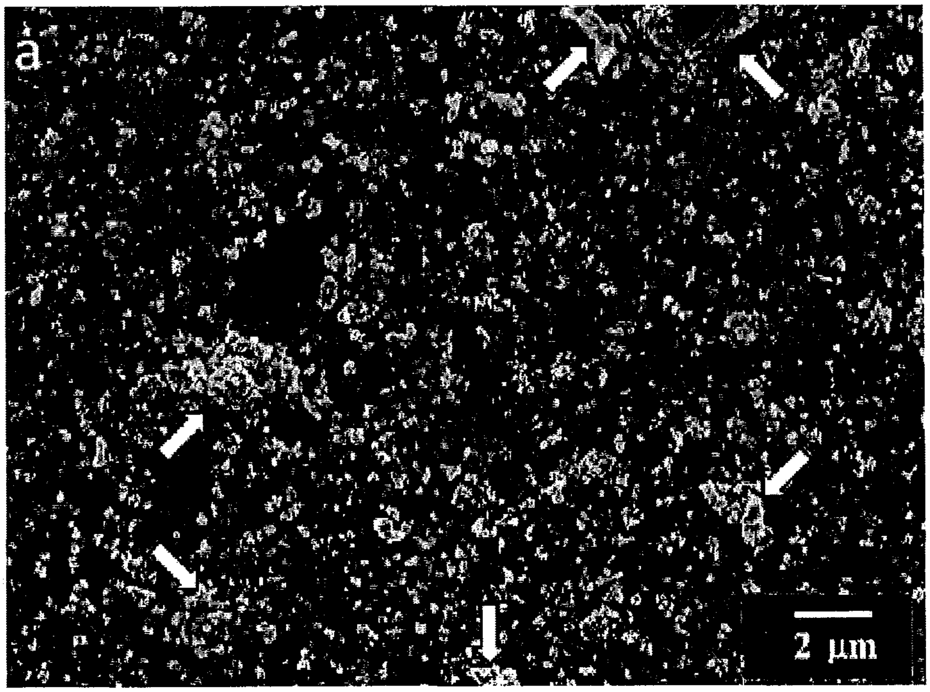

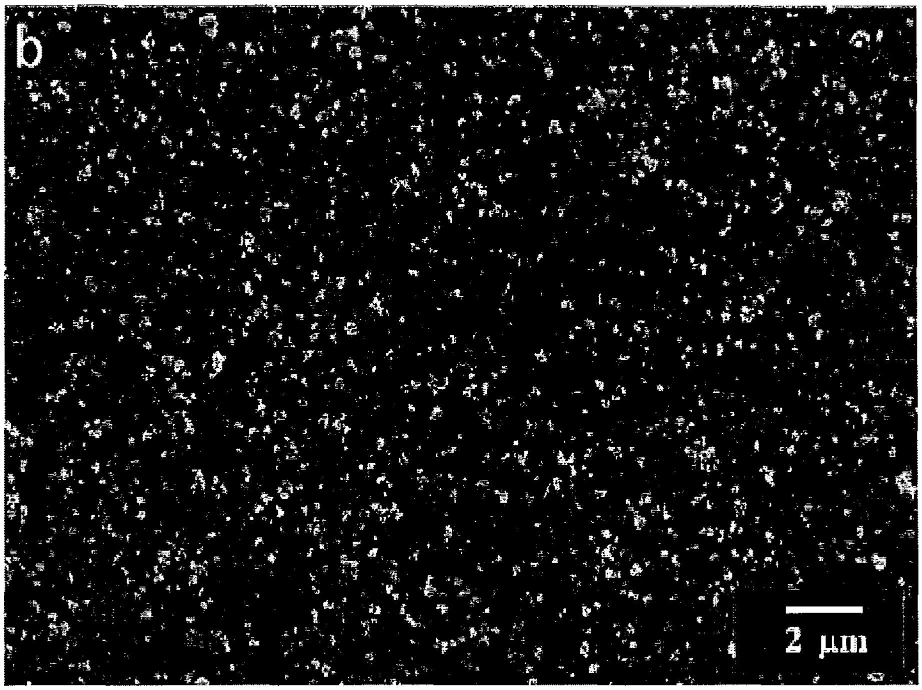

Figure 5-22 SEM images of the surfaces of the films deposited on the platinized silicon wafers from the 6 g/L PDAOT solutions, containing 4 g/L ZnO and (a) 0 g/L and (b) 0.01 g/L dopamine in a mixed ethanol–water solvent at the deposition voltage of 15 V (arrows show agglomerates of ZnO particles).

5.2.4.5 Effect of PDAOT and DA

The EPD of ceramic particles requires the use of efficient dispersants and binders.[93] In previous investigations [93, 105, 106] it was shown that various ceramic materials can be deposited by EPD using phosphate ester (PE) as a dispersant and polyvinyl butyral (PVB) as a binder. However, the use of PE as a dispersant can result in the contamination of ceramic deposits. Moreover, PE and PVB cannot be utilized for aqueous EPD. Another problem is related to the use of PVB, which has no charge and must be adsorbed on the charged ceramic particles, which provide electrophoretic transport of PVB to the electrode surface. Only adsorbed PVB was included in the deposits.[105, 106] Therefore, this approach enabled incorporation of small amounts of

PVB into the deposits and had a limited utility for the fabrication of composite materials. Other problems were related to the competitive adsorption of PE and PVB on the particle surface.

The use of DA as a dispersant, PDAOT as a binder and polymer matrix opens a new avenue in the EPD of ceramic particles and composites. Dispersion stability and particle charging are important factors for film fabrication by EPD. Ceramic particles and polymer macromolecules must be charged in the bulk of the suspensions. Electric charge promotes dispersion of particles and polymers and enables their electrophoretic motion towards the electrode surface. However, the electrostatic repulsion must be avoided at the electrode surface in order to achieve the film formation. Protonated DA and PDAOT exhibit a pH-dependent charge, which is beneficial for EPD. It is suggested that the deprotonation of the amino groups of DA and PDAOT in the high pH region at the cathode surface promoted deposit formation. DA and PDAOT can be used for EPD in aqueous or mixed solutions. Moreover, PDAOT has another advantage compared to electrically neutral PVB, as PDAOT is a cationic polymer and can be deposited independently. Using protonated PDAOT, dissolved in water or mixed water/ethanol solvent, water insoluble PDAOT films were obtained. The independent deposition of PDAOT enabled the formation of composite films, containing SWNTs or ZnO in the polymer matrix. It is suggested that PDAOT promotes dispersion and deposition of SWNTs. However, for the EPD of composite films with relatively large ZnO content, it was beneficial to use DA as a dispersant in order to avoid particle agglomeration.

The use of PDAOT with excellent binding and film forming properties enabled the formation of composite films. It should be noted that the formation of ceramic deposits by EPD presents difficulties attributed to the sintering stage. Sintering of ceramic deposits causes various problems, including the thermal degradation and oxidation of electrodes, changes in deposit composition related to the diffusion at the electrode–deposit interface. Other problems are related to the deposit cracking related to the sintering shrinkage and changes in material microstructure due to the grain growth at elevated temperatures. In contrast, the use of PDAOT offers the advantages of room temperature processing of nanocomposite materials. Recent studies showed that the adsorption of DA on the surfaces of oxide nanoparticles resulted in advanced optical and photovoltaic properties of the nanoparticles.[97, 98] The oxide nanoparticles containing adsorbed DA are currently under intensive investigation for application in advanced sensors, as well as optical and photovoltaic devices. Therefore the use of functional PDAOT binder and DA dispersant paves the way for the EPD of novel nanocomposites with advanced functional properties.

5.3 Electrodeposition of TiO_2 films using benzoic acid and phenolic molecules

TiO_2 suspensions in ethanol were unstable and showed a clear supernatant liquid 5 h after the ultrasonic agitation. No EPD was observed from such suspensions. In order to improve the suspension stability and achieve EPD of TiO_2, different organic additives were investigated. Figure 5-23 shows chemical structures of the additives used in this work. We utilized benzoic acid and phenolic compounds, which contained a different number of OH groups, bonded to the aromatic ring, and a COOH group.

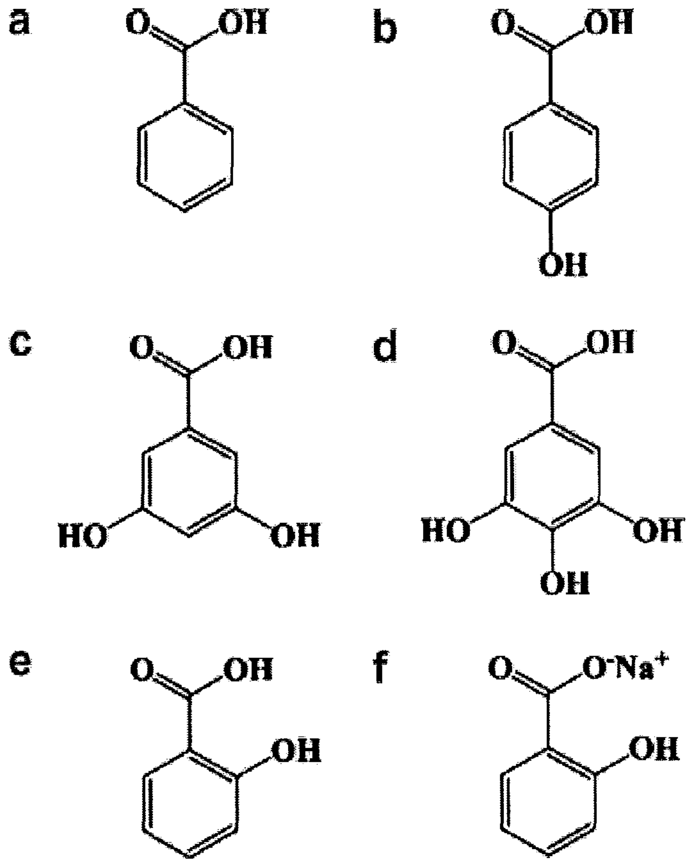

Figure 5-23 Chemical structures of: (a) benzoic acid, (b) 4-hydroxybenzoic acid, (c) 3,5-dihydroxybenzoic acid, (d) gallic acid, (e) salicylic acid and (f) salicylic acid sodium salt.

The dissociation of the organic molecules RCOOH resulted in the formation of anionic $RCOO^-$ species and H^+:

$$RCOOH \rightarrow RCOO^- + H^+ \qquad (5\text{-}4)$$

The charge of the TiO_2 particles in suspensions containing dissolved RCOOH was influenced by the competitive adsorption of $RCOO^-$ and H^+. The mechanism of $RCOO^-$

adsorption on the particles was influenced by OH and COO^- groups. The results obtained for the phenolic molecules with different number of OH groups were analyzed and compared with corresponding experimental data for the benzoic acid without OH groups. Moreover, the results presented below showed the effect of adjacent OH groups, as well as adjacent OH and COOH groups on adsorption of the organic molecules and EPD of oxide particles.

Sedimentation experiments showed that the addition of 4-hydroxybenzoic acid, 3,5-dihydroxybenzoic acid and salicylic acid sodium salt to the TiO_2 suspensions resulted in improved particle stability. The suspensions, containing benzoic acid and gallic acid showed significantly higher stability compared to the suspensions containing other additives and remained stable during 3–4 days after ultrasonic agitation. In contrast, no improvement in particle stability was observed after the addition of salicylic acid to the TiO_2 suspensions.

5.3.1 Cathodic deposition yield study of TiO_2 films

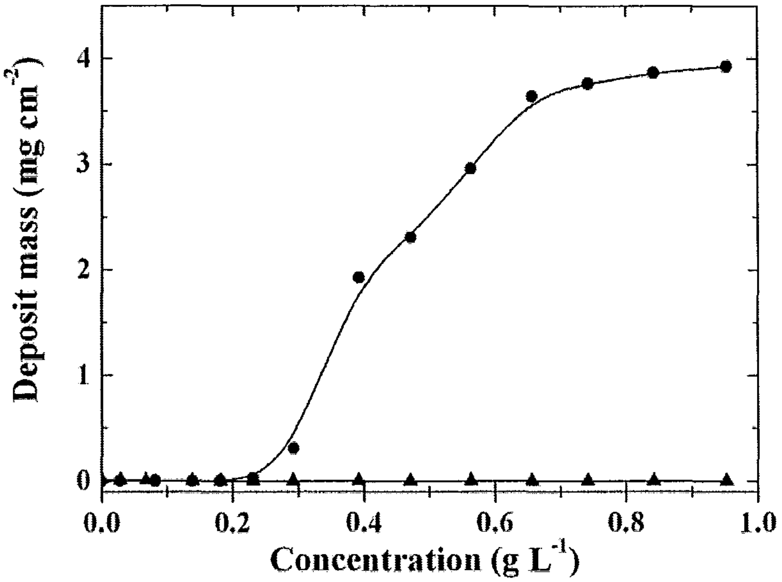

Figure 5-24 Deposit mass as a function of concentration of benzoic acid in 10 g/L TiO_2 suspension at a deposition voltage of 50 V with a deposition time of 2 min. (● – cathodic deposits, ▲– anodic deposits).

Figure 5-25 Possible coordination structures formed by chemisorption of (a and b) benzoic acid on TiO_2.

Cathodic deposits were obtained after the addition of 0.25 g/L benzoic acid to the TiO_2 suspensions. The deposition rate increased with increasing benzoic acid concentration in the suspensions (Figure 5-24). It is suggested that the dissociation of the benzoic acid resulted in the formation of anionic benzoate species and H^+. Therefore, the charge and electrokinetic behavior of the TiO_2 particles were influenced by competitive adsorption of the benzoate species and H^+ on the particle surfaces. The adsorption mechanism of benzoate on oxide particles can be attributed to the formation of mononuclear or binuclear chelates [117-120] between the COOH group and surface atoms (Figure 5-25a and b). However, the cataphoretic behavior of the TiO_2 particles in the suspensions containing benzoic acid indicated preferred adsorption of H^+ and the formation of positively charged particles.

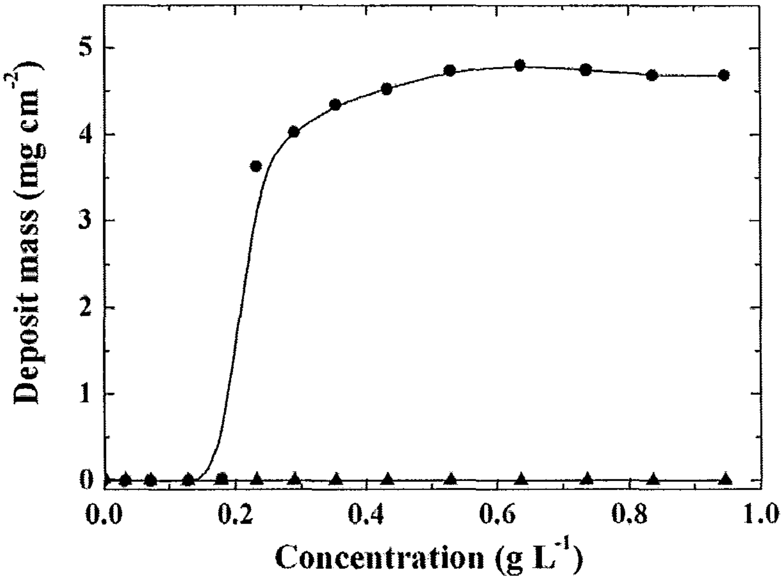

Figure 5-26 Deposit mass as a function of concentration of 4-hydroxybenzoic acid in 10 g/L TiO_2 suspension at a deposition voltage of 50 V with a deposition time of 2 min. (● – cathodic deposits, ▲– anodic deposits).

Cathodic deposits were also obtained from the TiO_2 suspensions containing 4-hydroxybenzoic acid and 3,5-dihydroxybenzoic acid. The deposition rate increased with increasing concentration of the organic additives (Figure 5-26 and Figure 5-27). It should be noted that the chemical structure of 4-hydroxybenzoic acid (Figure 5-23b) includes COOH and OH groups. However, the investigation of the deposition yield showed similar results for benzoic acid without OH group and 4-hydroxybenzoic acid containing OH group (Figure 5-24 and Figure 5-26). It was suggested that individual OH groups had no appreciable effect on the adsorption of the phenolic molecules. This is in good agreement with literature data, which showed weak adsorption of phenol on TiO_2[121]. The presence of an additional OH group in para position in 3,5-dihydroxybenzoic acid (Figure 5-23c) has no appreciable effect on the deposition yield data (Figure 5-27). However, the additional OH group in ortho position in the structure of gallic acid (Figure 5-23d) resulted in different electrophoretic behavior of TiO_2 particles in suspensions containing gallic acid as an additive.

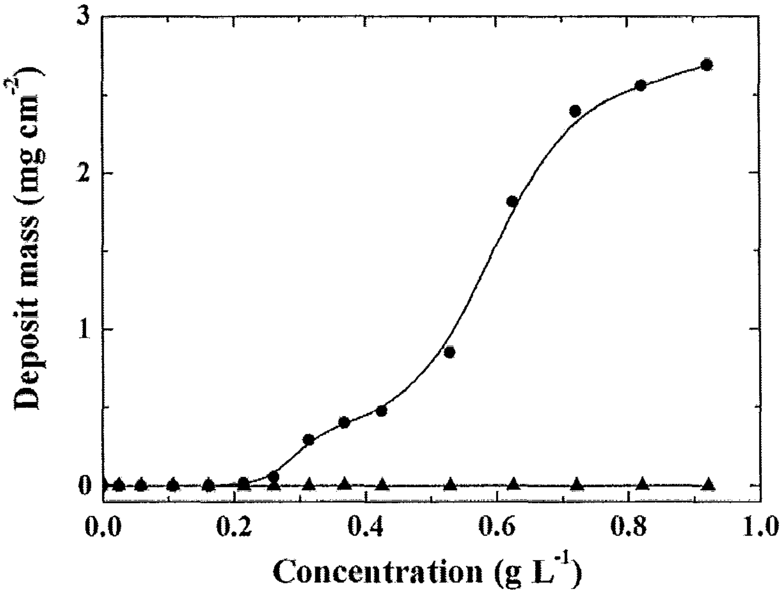

Figure 5-27 Deposit mass as a function of concentration of 3,5-dihydroxybenzoic acid in 10 g/L TiO_2 suspension at a deposition voltage of 50 V with a deposition time of 2 min. (● – cathodic deposits, ▲– anodic deposits).

5.3.2 Anodic deposition yield study of TiO_2 films

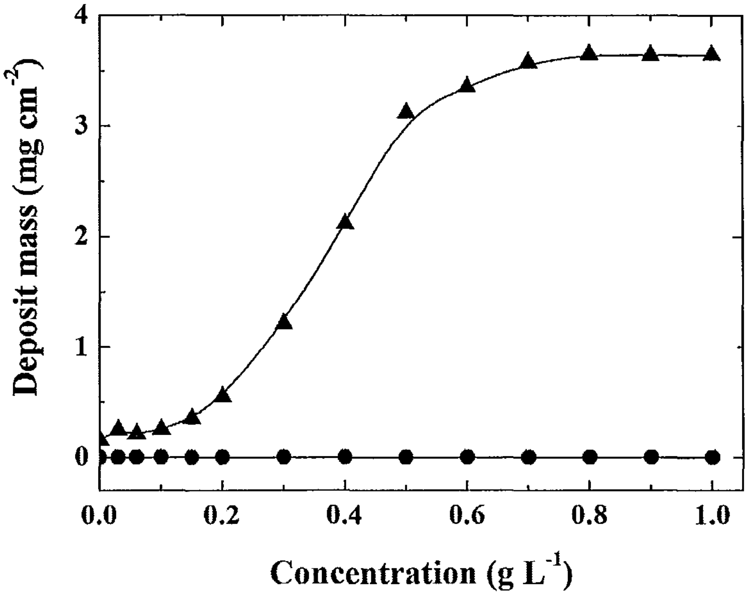

Figure 5-28 Deposit mass as a function of concentration of gallic acid in 10 g/L TiO_2 suspension at a deposition voltage of 50 V with a deposition time of 2 min. (● – cathodic deposits, ▲– anodic deposits).

The addition of gallic acid to the TiO_2 suspensions resulted in anodic deposition, which indicate that TiO_2 particles were negatively charged in the suspensions. The anodic deposition yield increased with increasing concentration of gallic acid, as shown in Figure 5-28. However, no deposition on the cathode was observed. The dissociation of gallic acid resulted in the formation of anionic gallate and H^+ and their competitive adsorption on the TiO_2 surface. It was suggested that the negative charge of the TiO_2 particles was attributed to preferred adsorption of anionic gallate. The comparison of the structures of benzoic acid, 4-hydroxybenzoic acid, 3,5-dihydroxybenzoic acid and gallic acid indicate that strong adsorption of gallate was attributed to the adjacent OH groups. This is in a good agreement with the literature data on the adsorption of catechol and related compounds containing adjacent OH groups [71]. According to the literature data on biomimetic adhesion, the strong adhesion of mussel adhesive proteins to metals and metal oxides is attributed to the chelation of catecholic amino acid, L-3,4-dihydroxyphenylalanine (DOPA) [122-124]. These studies showed strong DOPA adsorption on different surfaces. The strong affinity between catechol and metal oxides originates from the reaction between OH groups that are linked to surface metal atoms and the adjacent OH groups in catechol [71, 125, 126]. Figure 5-29a and b show proposed coordination structures for the catecholate type binding of gallic acid to the TiO_2 surface.

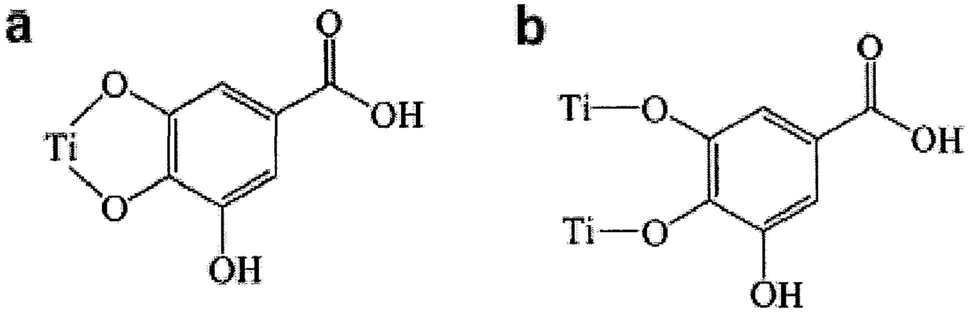

Figure 5-29 Possible coordination structures formed by chemisorption of (a and b) gallic acid on TiO_2.

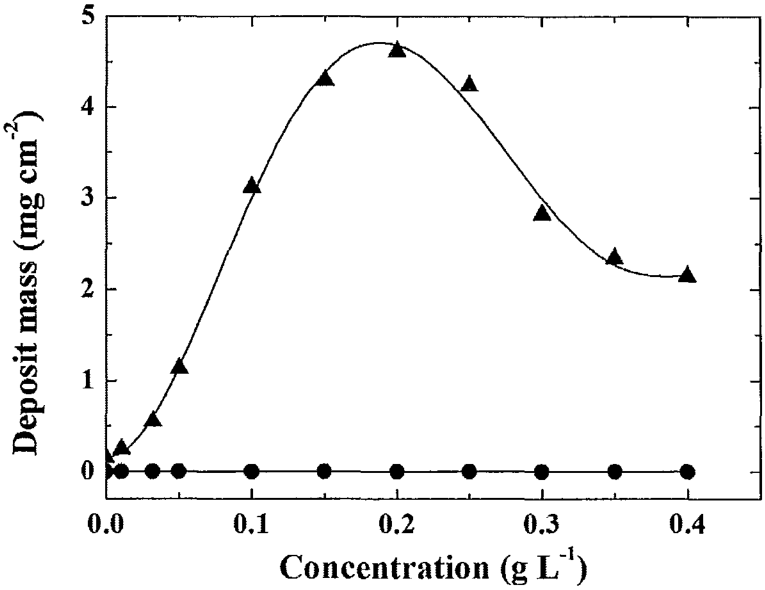

Figure 5-30 Deposit mass as a function of concentration of salicylic acid sodium salt in 10 g/L TiO_2 suspension at a deposition voltage of 50 V with a deposition time of 2 min. (● – cathodic deposits, ▲– anodic deposits).

The electrokinetic behavior of the TiO_2 particles in the suspensions containing salicylic acid or sodium salicylate was governed by the competitive adsorption of anionic salicylate and cationic H^+ or Na^+. The mechanism of the salicylate adsorption [109, 126] is related to the formation of mononuclear or binuclear complexes (Figure 5-31a and b). The TiO_2 suspensions containing salicylic acid were unstable and no EPD was observed from such suspensions. In contrast, anodic deposition was observed from TiO_2 suspensions containing sodium salicylate. The deposition rate increased with increasing concentration of sodium salicylate, showed a maximum at a concentration of 0.2 g/L and then decreased (Figure 5-30). The formation of anodic deposits indicated that TiO_2 particles were negatively charged owing to the preferred adsorption of salicylate anions. The increase in the sodium salicylate concentration above 0.2 g/L resulted in reduced suspension stability. It was suggested that the increase in sodium salicylate concentration in the TiO_2 suspensions resulted in increasing concentration of Na^+ ions, which promoted particle flocculation in agreement with the DLVO theory, Schulze–Hardey and Hofmeister rules [93]. The results described above indicate that adjacent OH groups of gallate as well as adjacent OH and COOH groups of salicylate provided strong adsorption of the organic molecules on the TiO_2 particles. The adsorption of the anionic ligands resulted in negative charge of the particles and allowed their anodic deposition. The use of gallic acid offered the advantage of higher suspension stability.

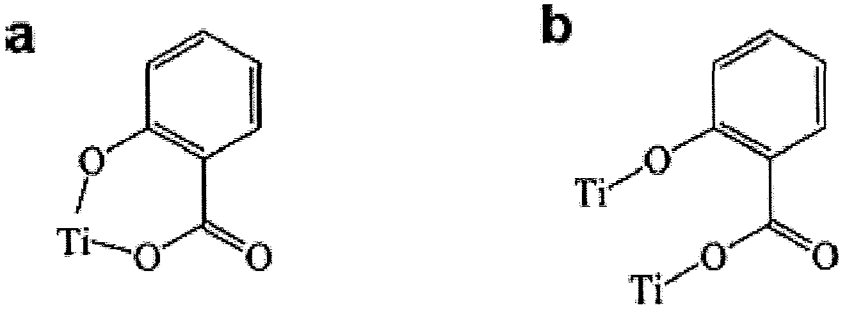

Figure 5-31 Possible coordination structures formed by chemisorption of (a and b) salicylic acid on TiO_2.

5.3.3 FTIR study of TiO_2 composite films

5.3.3.1 FTIR study of TiO_2 benzoic acid composite films

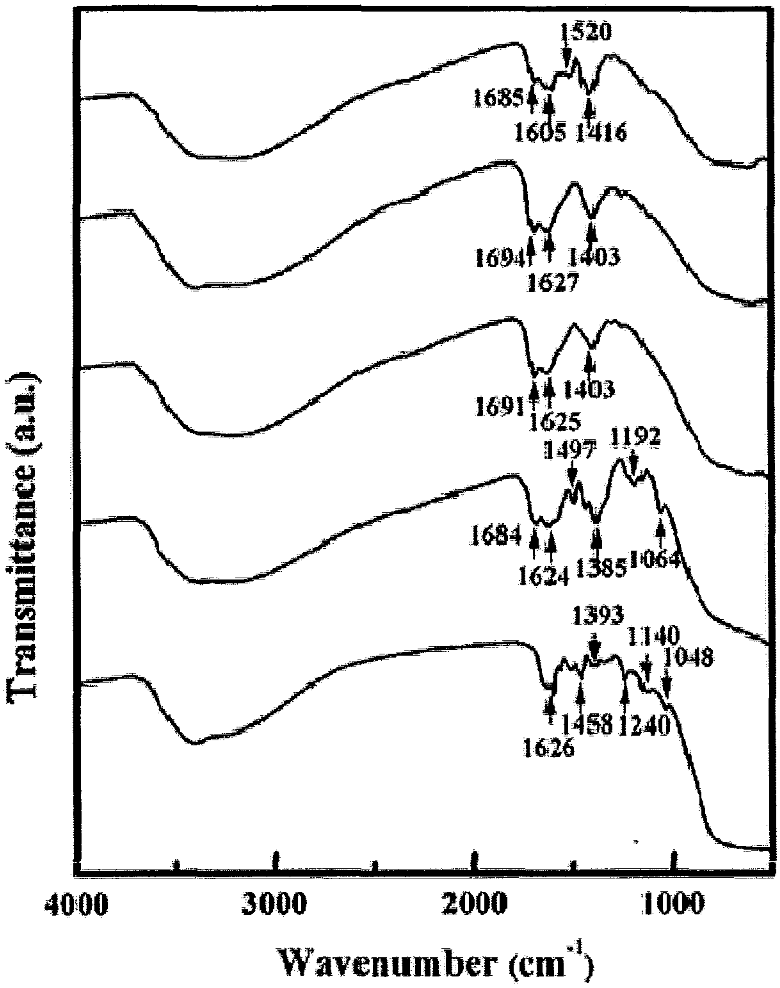

Figure 5-32 FTIR spectra for deposits prepared from 10 g/L TiO2 suspension containing (a) 1 g/L benzoic acid, (b) 1 g/L 4-hydroxybenzoic acid, (c) 1 g/L 3,5-dihydroxybenzoic acid, (d) 1 g/L gallic acid, (e) 0.4 g/L salicylic acid sodium salt at a deposition voltage of 50 V

FTIR spectrum of TiO_2 deposits, obtained from the suspension containing benzoic acid (Figure 5-32a), showed adsorption at 1685 cm^{-1}, which can be attributed to C=O stretching vibration of adsorbed benzoic acid [117]. The adsorption at 1605 cm^{-1} was attributed to C–C ring vibrations [110, 117]. The bands at 1520 and 1416 cm^{-1} were related to asymmetric and symmetric stretching vibrations of carboxyl group [117]. Therefore, the FTIR results showed adsorption of benzoic acid on TiO_2 particles. It is known that the adsorption of benzoic acid on the TiO_2 surface is attributed to the formation of a chelate between a carboxyl group and a surface Ti atom[117]. However, according to the literature[117], such adsorption is relatively weak. It is in this regard that our EPD data revealed the cathodic deposition of TiO_2 particles, which were positively charged due to the preferred adsorption of H^+.

5.3.3.2 FTIR study of TiO_2 4-hydroxybenzoic acid and 3,5-dihydroxybenzoic acid composite films

FTIR studies showed adsorption of 4-hydroxybenzoic acid and 3,5-dihydroxybenzoic acid on TiO_2 particles. The FTIR spectrum of the TiO_2 deposit prepared in the presence of 4-hydroxybenzoic acid showed adsorptions at 1694, 1627 and 1403 cm^{-1}, attributed to C=O stretching, C–C ring and carboxyl group vibrations, respectively (Figure 5-32b). Similar results were obtained for the TiO_2 deposit prepared using 3,5-dihydroxybenzoic acid (Figure 5-32c).

5.3.3.3 FTIR study of TiO_2 gallic acid composite films

The FTIR spectrum of the deposit prepared from TiO_2 suspension containing gallic acid is shown in Figure 5-32d. The main bands and their assignments are as-follows [116, 125, 126]: C=O stretching vibrations at 1684 cm^{-1}, C–C ring vibrations at 1624 cm^{-1}, asymmetric and symmetric stretching vibrations of carboxyl group at 1497 and 1385 cm^{-1}, bending vibrations of C–OH groups at 1192 cm^{-1} and aryl-oxygen stretching vibrations at 1064 cm^{-1}.

5.3.3.4 FTIR study of TiO_2 salicylic acid sodium salt composite films

The FTIR spectrum of the TiO_2 deposit prepared using salicylic acid sodium salt (Figure 5-32e) showed peaks assigned as-follows [103, 109, 110, 126]: C–C ring vibrations at 1626 and 1458 cm^{-1}, stretching vibrations of carboxyl group at 1393 cm^{-1}, C=O stretching of the salicylate ion at 1240 cm^{-1}, C–H in-plane bending at 1140 cm^{-1}, aryl-oxygen stretching vibrations at 1048 cm^{-1}.

5.3.3.5 Color changing of TiO_2 composite films

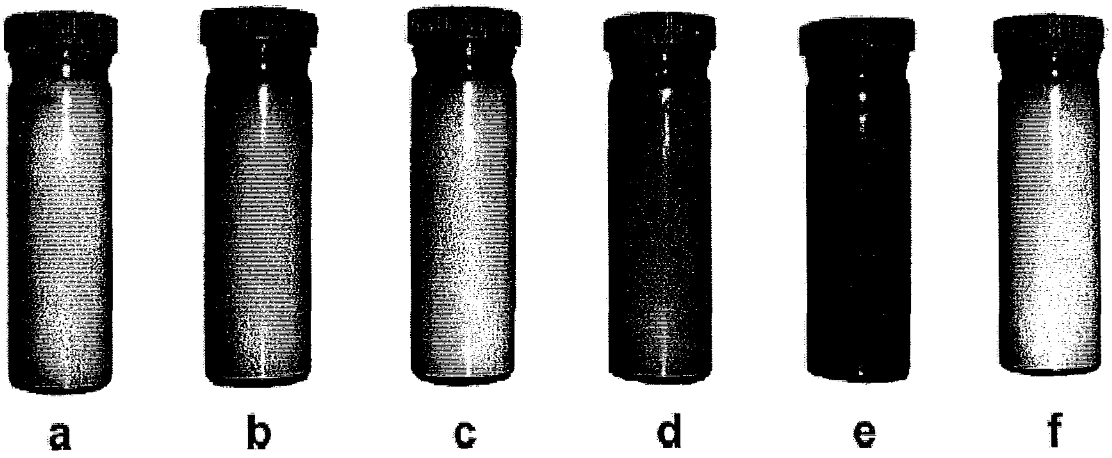

Figure 5-33 10 g/L TiO_2 suspensions: (a) without additives and containing, (b) 1 g/L benzoic acid, (c) 1 g/L 4-hydroxybenzoic acid, (d) 1 g/L 3,5-dihydroxybenzoic acid, (e) 1 g/L gallic acid, (f) 0.4 g/L salicylic acid sodium salt.

Figure 5-33 shows TiO_2 suspensions without additives and containing different additives. The TiO_2 suspensions showed changes in color from white for pure TiO_2 to light-pink, pink or light-yellow in the presence of 4-hydroxybenzoic acid, 3,5-dihydroxybenzoic acid and salicylic acid sodium salt, respectively. The suspensions containing gallic acid were brown. The changes in color can be attributed to the adsorption of organic molecules. It is known that adsorption of organic molecules from phenol family can result in materials with modified optical and semiconducting properties, which arise from the ligand-to-metal charge transfer interactions [71, 126]. It is important to note, that in this investigation charged phenolic molecules were utilized. Such additives can be used not only for the modification of materials properties, but also for electrostatic stabilization of the nanoparticles in suspensions and film fabrication by EPD.

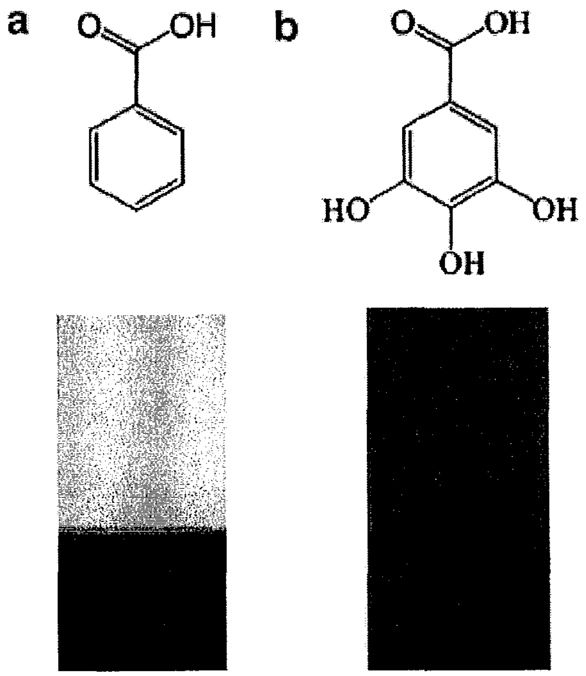

Figure 5-34 TiO_2 films prepared by: (a) cathodic and (b) anodic EPD on stainless steel substrates from 10 g/L TiO_2 suspensions, containing (a) 1 g/L benzoic acid and (b) 1 g/L gallic acid. The comparison of the chemical structures of (a) benzoic acid and (b) gallic acid indicates the influence of OH groups on adsorption of the organic molecules and charge of TiO_2 particles.

Figure 5-34 shows TiO_2 deposits on stainless steel substrates prepared from TiO_2 suspensions containing benzoic acid and gallic acid. The corresponding chemical structures are presented in order to show the influence of OH groups on the adsorption of the organic molecules and EPD of TiO_2. The TiO_2 films were deposited cathodically from suspensions containing benzoic acid. As pointed out above, the TiO_2 particle charge is attributed to H^+ adsorption. In contrast, the OH groups of gallic acid provided complexation of the surface Ti atoms and enabled the adsorption of anionic gallate on the particle surfaces. As a result, the TiO_2 particles were negatively charged and formed anodic deposits from the TiO_2 suspensions, containing gallic acid. The adsorption of gallic acid resulted in a color change from white (Figure 5-34a) to brown (Figure 5-34b). The results of this investigation indicated that gallic acid is a promising charging additive and dispersing agent for the anodic deposition of TiO_2. The important property of a charging additive for EPD of oxide materials is the ability of efficient charging of different materials.

6 Conclusions

The main conclusions are summarized as follows:

New electrochemical deposition methods have been developed for the fabrication of advanced composite coatings on metallic substrates.

- Cathodic EPD has been utilized for the fabrication of PDAOT, PDAOT-SWNTs composites, in which PDAOT is assigned as the electron donor and SWNTs are assigned as the electron acceptor. Also PDOAT-ZnO composites for hybrid organic solar cells have been deposited. The mechanism of cathodic deposition of the composites was based on the electrophoresis of protonated PDAOT and positively charged ZnO in acidic solutions and film formation in the high pH region at the cathode.
- PDAOT and co-deposition of PDAOT and PDAFP were co-deposited as monolayer composites or multilayers, containing layers of individual polymers using cathodic EPD. The mechanism was based on the electrophoresis of protonated PDAOT and PDAFP and film formation in the high pH region.
- The EPD method has been developed for the deposition of ZnO and TiO_2 nanoparticles. It was shown that cationic DA and anionic AY can be used as charging additives and dispersants. The adsorption mechanism was based on the complexation of the metal ions at the nanoparticle surfaces. DA was used for cathodic deposition of ZnO and TiO_2. The adsorption of AY on the ZnO

nanoparticles resulted in charge reversal and enabled the formation of anodic deposits. The use of DA as a common charging additive enabled the codeposition of ZnO and TiO_2 nanoparticles. The deposit composition and deposition yield can be varied by the variation of the suspension composition and deposition time. The EPD method can be used for the fabrication of nanostructured composite films.

- The electrophoretic deposition (EPD) method has been developed for the fabrication of TiO_2 films. Benzoic acid and phenolic molecules, such as 4-hydroxybenzoic acid, 3,5-dihydroxybenzoic acid, gallic acid, salicylic acid and salicylic acid sodium salt were investigated as additives for the dispersion and charging of TiO_2 particles. The adsorption of the organic molecules on the oxide particles involved the interaction of COOH groups and OH groups with metal atoms on the particle surfaces and complexation. Cathodic deposits were obtained from the suspensions containing benzoic acid, 4-hydroxybenzoic acid, 3,5-dihydroxybenzoic acid. Anodic deposits were obtained from the suspensions containing gallic acid and salicylic acid sodium salt. The results of deposition yield studies and FTIR investigation showed that adjacent OH groups, as well as adjacent OH and COOH groups bonded to the aromatic ring of the phenolic molecules enabled enhanced adsorption of the molecules on oxide particles. Gallic acid was shown to be an effective charging additive, which provided stabilization of TiO_2 particles in the suspensions and their deposition. Such organic molecules can be used for the dispersion and charging of oxide particles and for EPD of oxide films with advanced functional properties.

7 References

1. S. E. Shaheen, D.S.G., and G. E. Jabbour, *Organic-Based Photovoltaics: Toward Low-Cost Power Generation.* MRS Bull, 2005. **30**(10).
2. Carson, J.A., *Solar cell research progress.* 2008: New York : Nova Science Publishers. 331.
3. *March 2009 issue of Photon International.*
4. Green, M.A., *Third generation photovoltaics: solar cells for 2020 and beyond.* Physica E: Low-dimensional System and Nanostructures, 2002. **14**: p. 11-17.
5. Green, M.A., *Third generation photovoltaics: solar cells for 2020 and beyond.* Physica E: Low-dimensional System and Nanostructures, 2002. **14**: p. 65-70.
6. *Highest Silicon Solar Cell Efficiency Ever Reached.* 2008.
7. K. L. Chopra, P.D.P.a.V.D., *Thin-Film Solar Cells: An Overview.* Prog. Photovolt: Res. Appl., 2004. **12**: p. 69-92.
8. N. Romeoa, A.B., V. Canevarib and A. Podestà, *Recent progress on CdTe/CdS thin film solar cells.* Solar Energy, 2004. 77(6): p. 795-801.
9. Wu X, K.J., Dhere RG, DeHart C, Duda A, Gessert TA, Asher S, Levi DH, Sheldon P, *16.5% Efficient CdS/CdTe polycrystalline thin-film solar cells*, in *Proceedings of the 17th European Photovoltaic Solar Energy Conference.* 2001. p. 995-1001.
10. De Vos A, P.J., Baruch P, Landsberg PT, *Bandgap effects in thin-film heterojunction solar cells*, in *Proceedings of the 12th European Photovoltaic Solar Energy Conference.* 1994. p. 1315-1318.
11. Hedstro¨m J, O.n.H., *ZnO/CdS/Cu(In,Ga)Se2 thin-film solar cells with improved performance*, in *Proceedings of the 23rd IEEE Photovoltaic Specialists Conference.* 1993. p. 364-371.
12. Shafarman WN, K.R., McCandless BE, *Device and material characterization of Cu(InGa)Se2 solar cells with increasing band gap.* Journal of Applied Physics, 1996. **79**: p. 7324-7328.
13. Ramanathan K, C.M., Perkins CL, Asher S, Hasoon FS, Keane J, Young D, Romero M, Metzger W, Noufi R, and D.A. Ward J, *Properties of 19.2% efficiency ZnO/CdS/CuInGaSe2 thin-film solar cells.* Progress in Photovoltaics Research and Applications, 2003. **11**: p. 225-230.
14. Jones, M.R. *Schematic illustration of a generic dye-sensitized solar cell.* 2009; Available from: http://upload.wikimedia.org/wikipedia/commons/f/fd/Dye_Sensitized_Solar_Cell_Scheme.png.
15. Society, A.C., *Ultrathin, Dye-sensitized Solar Cells Called Most Efficient To Date.* ScienceDaily, 2006.
16. Gao, F.W., Y; Zhang, J; Shi, D; Wang, M; Humphry-Baker, R; Wang, P; Zakeeruddin, Sm; Grätzel, M, *A new heteroleptic ruthenium sensitizer enhances the absorptivity of mesoporous titania film for a high efficiency dye-sensitized solar cell.* Chemical communications, 2008. **23**: p. 2635-2641.
17. *Solarmer Energy, Inc. Breaks Psychological Barrier with 8.13% OPV Efficiency.* Available from: http://finance.yahoo.com/news/Solarmer-Energy-Inc-Breaks-bw-3898683911.html?x=0&.v=1.
18. Filippelli, G.C.a.L., *Organic Solar Cells: Problems and Perspectives.* International Journal of Photoenergy, 2010: p. 11.
19. N.P, R., in *Leading edge research in solar energy.* 2007.

20. P. A. Troshin, R.N.L., and V. F. Razumov, *Organic Solar Cells: Structure, Materials, Critical Characteristics, and Outlook.* Nanotechnologies in Russia, 2008. **3**(5-6): p. 242-271.
21. Cheney, T., *NREL Confirms Spectrolab's 41.6% Conversion Efficiency Record.* 2009.
22. W. Shockley, H.J.Q., *Detailed balance limit of efficiency of p-n junction solar cells.* Journal of Applied Physics, 1961. **32**(3): p. 510.
23. al., M.A.G.e., *Solar cell efficiency tables (Version 29).* Progress in Photovoltaics, 2007.
24. C.B. Honsberg, R.C., and S.P. Bremner, *A new generalized detailed balance formulation to calculate solar cell efficiency limits*, in *17th Photovoltaic European Conference.* 2001.
25. Burnett, B., *The basic physics and design of III-V multijunction solar cells.* 2002.
26. al., F.D.e., *Next generation GaInP/GaInAs/Ge multi-junction space solar cells*, in *17th Photo-voltaic European Conference.* 2001.
27. Román, J.M., *State-of-the-art of III-V solar cell fabrication technologies, device designs and applications.* Advanced Photovoltaic Cell Design, 2004.
28. J.M.Olson, D.J.F., S.Kurtz, *High-Efficiency III-V Multijunction Solar Cells*, in *Handbook of Photovoltaic Science and Engineering.* 2003.
29. Rostalski, J.M., D, *Monochromatic versus solar efficiencies of organic solar cells.* Sol. Energy Mater. Sol. Cells, 2000. **61**: p. 87.
30. Parker, I., *Carrier Tunneling and Device Characteristics in Polymer Light-emitting-diodes.* Journal of Applied Physics, 1994. **75**: p. 1656-1666.
31. Brabec, C.J.C., A.; Meissner, D.; Sariciftci, N. S.; Fromherz, and M.S. T.; Minse, L.; Hummelen, J. C, *Origin of the Open Circuit Voltage of Plastic Solar Cells.* Advanced Functional Materials, 2001. **11**(5): p. 374-380.
32. Scharber, M.M.h., D.; Koppe, M.; Denk, P.; Waldauf, C.; Heeger, A. J.; Brabec, C, *Design Rules for Donors in Bulk-Heterojunction Solar Cells—Towards 10% Energy-Conversion Efficiency.* Advanced Functional Materials, 2006. **18**: p. 789-794.
33. Hoppe, H.S., N. S, *Organic solar cells: an overview.* Journal of Materials Research, 2004. **19**: p. 1924-1945.
34. Serap Gu¨nes, H.N., and Niyazi Serdar Sariciftci, *Conjugated Polymer-Based Organic Solar Cells.* Chemistry reviews, 2007. **107**: p. 1324-1338.
35. Van Duren, J.Y., X.; Loos, J.; Bulle-Lieuwma, C. W. T.; Sievel, A. B.; Hummelen, J. C.; Janssen, R. A. J, *Relating the Morphology of Poly(p-phenylene vinylene)/Methanofullerene Blends to Solar-Cell Performance* Advanced Functional Materials, 2004. **14**: p. 425-434.
36. Hoppe, H.G., T.; Niggemann, M.; Schwinger, W.; Schaeffler, F.; Hinsch, A.; Lux-Steiner, M.; Sariciftci, N. S., *Efficiency limiting morphological factors of MDMO-PPV:PCBM plastic solar cells.* Thin Solid Films, 2006. **511-512**: p. 587-592.
37. Hoppe, H.N., M.; Winder, C.; Kraut, J.; Hiesgh, R.; Hinsch, A.; Meissner, D.; Sariciftci, N. S., *Nanoscale Morphology of Conjugated Polymer/Fullerene-Based Bulk- Heterojunction Solar Cells.* Advanced Functional Materials, 2004. **14**: p. 1005-1011.
38. Arias, A.C.M., J. D.; Stevenson, R.; Halls, J. M.; Inbasekaran, M.; Woo, E. P.; Richards, D.; Friend, R. H., *Photovoltaic Performance and Morphology of Polyfluorene Blends: A Combined Microscopic and Photovoltaic Investigation.* Macromolecules, 2001. **34**: p. 6005.

39. Gadisa, A., *Correlation between oxidation potential and open-circuit voltage of composite solar cells based on blends of polythiophenes/ fullerene derivative.* Applied Physics Letters, 2004. **84**(1609).
40. Riedel, I.D., V, *Influence of electronic transport properties of polymer-fullerene blends on the performance of bulk heterojunction photovoltaic devices.* Physica Status solidi (a), 2004. **201**: p. 1332-1341.
41. Maenning, B.D., J.; Gebeyehu, D.; Simon, P.; Kozlowski, F.; Werner, A.; Li, F.; Gundmann, S.; Sonntag, S.; Koch, M.; Leo, K.; Pfeiffer, M.; Hoppe, H.; Meissner, D.; Sariciftci, S.; Riedel, I.; Dyakonov, V.; Parisi, J, Journal of Applied Physics, 2004. **79**: p. 1.
42. A.C. Arias, K.P., M. Granstrom, J.J. Dittmer, E.A. Marseglia and R. H. Friend, *Efficient Polymeric Photovoltaic Devices*, in *Proc. CBECIMAT.* 1998.
43. Halls, J.J.M., *Photoconductive properties of conju- gated polymers.* 1997, Cambridge.
44. Friend, K.P.a.R.H., *Ultrathin Organic Pho- tovoltaic Devices.* Synthetic Metals, 1999. **102**: p. 976.
45. Kietzke, T., *Recent Advances in Organic Solar Cells.* Advances in OptoElectronics, 2007. **2007**: p. 40285.
46. Petritsch, D.I.K., *Organic Solar Cell Architectures.* 2000, Cambridge and Graz.
47. Tang, C.W., *Two-Layer Organic Photovoltaic Cell.* Applied Physics Letters, 1986. **48(2)**: p. 183-185.
48. C. Jonda, A.B.R.M., U. Stolz, A. Elschner and A. Karbach, *Surface roughness effects and their influence on the degradation of organic light emitting devices.* Journal of Materials Science, 2000. **35**: p. 5645-5651.
49. A. Elschner, F.B., H. W. Heuer, F. Jonas, A. Karbach, S. Kirchmeyer and S. Thurm, *PEDT/PSS for efficient hole-injection in hybrid organic light-emitting diodes.* Synthetic Metals, 2000. **111**: p. 139-143.
50. Alam, M.M.a.S.A.J., *Efficient Solar Cells from Layered Nanostructures of Donor and Acceptor Conjugated Polymers.* Chemistry of Materials, 2004. **16**: p. 4647-4656.
51. Koetse, M.M., et al., *Efficient polymer:polymer bulk heterojunction solar cells.* Applied Physics Letters, 2006. **88**: p. 083504.
52. Kietzke, T., et al., *Comparative Study of M3EH-PPV-Based Bilayer Photovoltaic Devices.* Macromolecules, 2006. **39**: p. 4018-4022.
53. Shaheen, S.B., C. J.; Sariciftci, N. S.; Padinger, F.; Fromherz, T.; Hummelen, J. C., *2.5% efficient organic plastic solar cells.* Applied Physics Letters, 2001. **78**: p. 841-843.
54. Wienk, M.M., et al., *Efficient methano[70]fullerene/MDMO-PPV bulk heterojunction photovoltaic cells.* Angewandte Chemie-International Edition, 2003. **42**: p. 3371-3375.
55. Li, G., et al., *High-efficiency solution processable polymer photovoltaic cells by self-organization of polymer blends.* Nature Materials, 2005. **4**: p. 864-868.
56. Reyes-Reyes, M., K. Kim, and D.L. Carroll, *High-efficiency photovoltaic devices based on annealed poly(3-hexylthiophene) and 1-(3-methoxycarbonyl)-propyl-1- phenyl-(6,6)C[sub 61] blends.* Applied Physics Letters, 2005. **87**: p. 083506.
57. Ma, W., et al., *Thermally stable, efficient polymer solar cells with nanoscale control of the interpenetrating network morphology.* Advanced Functional Materials, 2005. **15**: p. 1617-1622.

58. J. Y. Kim, K.L., N. E. Coates, et al., *Efficient Tandem Polymer Solar Cells Fabricated by All-Solution Processing.* Science (Washington), 2007. **317**: p. 222-225.

59. Sariciftci, N.S., et al., *Photoinduced Electron Transfer from a Conducting Polymer to Buckminsterfullerene.* Science, 1991. **258**: p. 1474.

60. Shaheen, S.E., et al., *2.5% efficient organic plastic solar cells.* Applied Physics Letters, 2001. **78**: p. 841-843.

61. PAUL HEREMANS, D.C., AND BARRY P. RAND, *Strategies for Increasing the Efficiency of Heterojunction Organic Solar Cells: Material Selection and Device Architecture.* Accounts of Chemical Research, 2009. **42**: p. 1740-1747.

62. Sariciftci, H.H.a.N.S., *Polymer Solar Cells.* Advances in Polymer Science, 2007. **12**: p. 121.

63. H. Ogata, R.H., and N. Kobayashi, *Electronic absorption spectra of substituted phthalocyanines in solution and as films.* Journal of Porphyrins and Phthalocyanines, 2003. **7**: p. 551-557.

64. R. D. George, A.W.S., J. S. Shirk, and W. R. Barger, *The alpha substitution effect on phthalocyanine aggregation.* Journal of Porphyrins and Phthalocyanines, 1998. **2**: p. 1-7.

65. Krebs, E.B.a.F.C., *Low band gap polymers for organic photovoltaics.* Solar Energy Materials and Solar Cells, 2007. **91**: p. 954-985.

66. G. P. Smestad, F.C.K., C. M. Lampert et al., *Reporting solar cell efficiencies in Solar EnergyMaterials and Solar Cells.* Solar Energy Materials and Solar Cells, 2008. **92**: p. 371-373.

67. R. F. Bailey-Salzman, B.P.R., and S. R. Forrest, *Nearinfrared sensitive small molecule organic photovoltaic cells based on chloroaluminum phthalocyanine.* Applied Physics Letters, 2007. **91**: p. 013508.

68. E. Holder, N.T.a.A.L.R., *Hybrid nanocomposite materials with organic and inorganic components for opto-electronic devices* Journal of Materials Chemistry, 2008. **18**: p. 1064-1078.

69. Turner, B.R.S.a.M.L., *Nanoparticle-polymer photovoltaic cells.* Advances in Colloid and Interface Science, 2008. **138**: p. 1-23.

70. Skompska, M., *Hybrid conjugated polymer/semiconductor photovoltaic cells.* Synthetic Metals, 2010. **160**: p. 1-15.

71. T. Rajh, L.X.C., K. Lukas, T. Liu, M. C. Thurnauer, and D. M. Tiede, *Surface Restructuring of Nanoparticles: An Efficient Route for Ligand-Metal Oxide Crosstalk.* Journal of Physical Chemistry, 2002. **106**: p. 10543-10552.

72. Yunfei Zhou, M.E.a.M.K., *Bulk-heterojunction hybrid solar cells based on colloidal nanocrystals and conjugated polymers.* Energy & Environmental Science 2010.

73. Alivisatos, A.P., *Semiconductor Clusters, Nanocrystals, and Quantum Dots.* Science, 1996. **271**: p. 933-937.

74. Alford, M.D.D.a.J.M., *Isolation and Properties of Small-Bandgap Fullerene.* Nature, 1998. **393**: p. 668-671.

75. S. Dayal, M.O.R., A. J. Ferguson, D. S. Ginley, G. Rumbles and N. Kopidakis, *The Effect of Nanoparticle Shape on the Photocarrier Dynamics and Photovoltaic Device Performance of Poly(3- hexylthiophene):CdSe Nanoparticle Bulk Heterojunction Solar Cells.* Advanced Functional Materials, 2010. **20**: p. 2629-2635.

76. Andr'e, J.S.a.J.J., *Molecular Semiconductors.* Springer, 1985.

77. J. J. M. Halls, K.P., R. H. Friend, S. C. Moratti and A. B. Holmes, *Exciton diffusion and dissociation in a poly(p - phenylenevinylene)/C60 heterojunction photovoltaic cell.* Applied Physics Letters, 1996. **68**: p. 3120-3122.

78. D. E. Markov, E.A., P. W. M. Blom, A. B. Sieval and J. C. Hummelen, *Accurate Measurement of the Exciton Diffusion Length in a Conjugated Polymer Using a Heterostructure with a Side-Chain Cross-Linked Fullerene Layer.* Journal of Physical Chemistry, 2005. **109**: p. 5266-5274.

79. Cheyns, D.V., K.; Rolin, C.; Genoe, J.; Poortmans, J.; Heremans, P., *Nanoimprinted semiconducting polymer films with 50 nm features and their application to organic heterojunction solar cells.* Nanotechnology, 2008. **19**: p. 424016.

80. Westenhoff, S.H., I. A.; Hodgkiss, J. M.; Kirov, K. R.; Bronstein, H. A.; Williams, C. K.; Greenham, N. C.; Friend, R. H., *Charge recombination in organic photovoltaic devices with high open-circuit voltages.* Journal of the American Chemical Society, 2008. **130**: p. 13653-13658.

81. Ohkita, H.C., S.; Astuti, Y.; Duffy, W.; Tierney, S.; Zhang, W.; Heeney, M.; McCulloch, I.; Nelson, J.; Bradley, D. D. C.; Durrant, J. R., *Charge carrier formation in polythiophene/fullerene blend films studied by transient absorption spectroscopy.* Journal of the American Chemical Society, 2008. **130**: p. 3030-3042.

82. Rand, B.P.B., D. P.; Forrest, S. R., *Offset energies at organic semiconductor heterojunctions and their influence on the open-circuit voltage of thin-film solar cells.* Physical Review, 2007. **75**: p. 115327.

83. Cheyns, D.P., J.; Heremans, P.; Deibel, C.; Verlaak, S.; Rand, B. P.; Genoe, J., *Analytical model for the open-circuit voltage and its associated resistance in organic planar heterojunction solar cells.* Physical Review, 2008. **77**: p. 165332.

84. Vandewal, K.G., A.; Oosterbaan, W. D.; Bertho, S.; Banishoeib, F.; Severen, I. V.; Lutsen, L.; Cleij, T. J.; Vanderzande, D.; Manca, J. V., *The relation between open-circuit voltage and the onset of photocurrent generation by charge-transfer absorption in polymer: fullerene bulk heterojunction solar cells.* Advanced Functional Materials, 2008. **18**: p. 2064-2070.

85. L. J. A. Koster, V.D.M., and P. W. M. Blom, *Ultimate Efficiency of Polymer/Fullerene Bulk Heterojunction Solar Cells.* Applied Physics Letters, 2006. **88**: p. 093511.

86. Rand, B.P.X., J.; Uchida, S.; Forrest, S. R., *Mixed donor-acceptor molecular heterojunctions for photovoltaic applications. I. Material properties.* Journal of Applied Physics, 2005. **98**: p. 124902.

87. E. Kymakis, I.A., and G. A. J. Amaratunga, *Photovoltaic cells based on dye-sensitisation of single-wall carbon nanotubes in a polymer matrix.* Solar Energy Materials and Solar Cells, 2003. **80**: p. 465-472.

88. V. D. Mihailetchi, J.K.J.v.D., P. W. M. Blom, J. C. Hummelen, R. A. J. Janssen, J. M. Kroon, M. T. Rispens, W. J. H. Verhees and M. A. Wienk, *Electron Transport in a Methanofullerene.* Advanced Functional Materials, 2003. **13**: p. 43-46.

89. Y. F. Zhou, F.S.R., Y. Yuan, H. F. Schleiermacher, M. Niggemann, G. A. Urban and M. Krueger, *Improved efficiency of hybrid solar cells based on non-ligand-exchanged CdSe quantum dots and poly(3-hexylthiophene).* Applied Physics Letters, 2010. **96**: p. 013304.

90. Rode, D.L., *Electron Mobility in Direct-Gap Polar Semiconductors.* Physical Review B: Solid State, 1970. **2**: p. 4036-4044.

91. FrederikC.Krebs, *Fabrication and processing o fpolymer solar cells: A review of printing and coating techniques.* Solar Energy Materials & Solar Cells, 2009. **93**: p. 394-412.

92. I. Zhitomirsky, M.N.a.A.P., *Electrodeposition of hybrid organic–inorganic films containing iron oxide.* Materials Letters, 2003. **57**: p. 1045-1050.

93. I. Zhitomirsky, *Cathodic Electrodeposition of Ceramic and Organoceramic Materials. Fundamental Aspects.* Advances in Colloid and Interface Science, 2002. **97**: p. 277.

94. M. Cheong, I.Z., *Electrodeposition of alginic acid and composite films.* Colloids and Surfaces A: Physicochemical and Engineering Aspects, 2008. **328**: p. 73.

95. Kangmin Wu, P.I., Alex Adronov, Igor Zhitomirsky, *Electrophoretic deposition of poly[3-(3-N,N-diethylaminopropoxy)thiophene] and composite films.* Materials Chemistry and Physics, 2010.

96. Moudgil, R.D.a.B.M., *Electrophoretic Deposition of Calcium Phosphates from Non-Aqueous Media.* Colloids and Surfaces A: Physicochemical and Engineering Aspects, 1993. **80**: p. 191.

97. G.-L. Wang, J.-J.X., H.-Y. Chen, Biosensors and Bioelectronics, 2009. **24**: p. 2494.

98. W. Huang, P.J., C. Wei, D. Zhuang, J. Shi, Journal of Materials Research, 2008. **23**: p. 1946.

99. D. Gutie'rrez-Tauste, X.D.n., C. Domingo, and J. A. Ayllo'n, *Dopamine/ TiO2 Hybrid Thin Films Prepared by the Liquid Phase Deposition Method.* Thin Solid Films, 2008. **516**: p. 3831.

100. I. Zhitomirsky, *Electrophoretic Hydroxyapatite Coatings and Fibers.* Materials Letters, 2000. **42**: p. 262.

101. Y. J. Kwon, K.H.K., C. S. Lim, and K. B. Shim, *Characterization of ZnO Nanopowders Synthesized by the Polymerized Complex Method Via an Organochemical Route.* Journal of Ceramic Processing Research, 2002: p. 146.

102. A. Umar, M.M.R., M. Vaseem, and Y.-B. Hahn, *Ultra-Sensitive Cholesterol Biosensor Based on Low-Temperature Grown ZnO Nanoparticles.* Electrochemistry Communications, 2009. **11**: p. 118.

103. P. A. Connor, K.D.D., and A. J. McQuillan, *New Sol-Gel Attenuated Total Reflection Infrared Spectroscopic Method for Analysis of Adsorption at Metal Oxide Surfaces in Aqueous Solutions. Chelation of TiO2, ZrO2, and Al2O3 Surfaces by Catechol, 8-Quinolinol, and Acetylacetone.* Langmuir, 2002. **11**: p. 4193.

104. M. D. Shultz, J.U.R., S. N. Khanna, and E. E. Carpenter, *Reactive Nature of Dopamine as a Surface Functionalization Agent in Iron Oxide Nanoparticles.* Journal of the American Chemical Society, 2007. **129**: p. 2482.

105. I.Zhitomirsky, A.P., *Electrophoretic deposition of ceramic materials for fuel cell applications.* Journal of the European Ceramic Society, 2000. **20**: p. 2055.

106. I. Zhitomirsky, A.P., *Electrophoretic deposition of electrolyte materials for solid oxide fuel cells.* Journal of Materials Science 2004. **39**: p. 825.

107. D. Philip, A.J., C. Y. Panicker, and H. T. Varghese, *FT-Raman, FT-IR and Surface Enhanced Raman Scattering Spectra of Sodium Salicylate.* Spectrochimica Acta Part A: Molecular and Biomolecular Spectroscopy, 2001. **57**: p. 1561.

108. Billes, I.M.-Z.a.F., *Vibrational Spectroscopic Calculations on Pyrogallol and Gallic Acid.* Journal of Molecular Structure: THEOCHEM, 2002. **618**: p. 259.

109. McQuillan, K.D.D.a.A.J., *In Situ Infrared Spectroscopic Analysis of the Adsorption of Aromatic Carboxylic Acids to TiO_2, ZrO_2, Al_2O_3, and Ta_2O_5 from Aqueous Solutions.* Spectrochimica Acta Part A: Molecular and Biomolecular Spectroscopy, 2000. **56**: p. 557.

110. X. Guan, G.C., and C. Shang, *ATR-FTIR and XPS Study on the Structure of Complexes Formed Upon the Adsorption of Simple Organic Acids on Aluminum Hydroxide.* Environmental Science & Technology, 2007. **19**: p. 438.

111. I.Zhitomirsky, L.G.-O., *Electrophoretic deposition of hydroxyapatite.* Journal of Materials Science: Materials in Medicine, 1997. **8**: p. 213.

112. I. Zhitomirsky, L.G.-O., *Formation of Hollow Fibers by Electrophoretic Deposition.* Materials Letters, 1999. **38**: p. 10.

113. K.D. Trimukhe, A.J.V., *Metal complexes of crosslinked chitosans: Correlations between metal ion complexation values and thermal properties* Carbohydrate Polymers, 2009. **75**: p. 63.

114. T. Yogo, T.N., M. Kachi, W. Sakamoto, S.-I. Hirano, *In Situ Synthesis of Nanosized ZnO Particle/Organic Hybrids.* Japanese Journal of Applied Physics, 2006. **45**: p. 6033.

115. C. Xu, K.X., H. Gu, R. Zheng, H. Liu, X. Zhang, Z. Guo, B. Xu, Journal of the American Chemical Society, 2004. **126**: p. 9938.

116. Y. Wang, I.Z., *Electrophoretic deposition of manganese dioxide-multiwalled carbon nanotube composites for electrochemical supercapacitors.* Langmuir, 2009. **25**: p. 9684.

117. S. Tunesi, M.A.A., *Surface effects in photochemistry: an in situ cylindrical internal reflection-Fourier transform infrared investigation of the effect of ring substituents on chemisorption onto titania ceramic membranes.* Langmuir, 1992. **8**: p. 487.

118. X.-h. Guan, G.-h.C., C. Shang, Journal of Environmental Sciences, 2007. **19**: p. 438.

119. C.A. Koutstaal, V.P., *FT-IR study on the adsorption of benzoic acid and its derivatives on transition-metal oxides* Applied Surface Science, 1993. **70-71**: p. 206.

120. H. Nishikiori, J.S., N. Takahashi, T. Takagi, N. Tanaka, T. Fujii, *Removal of detergents and fats from waste water using allophane.* Applied Clay Science, 2009. **43**: p. 160.

121. S. Bekkouche, M.B., N.H. Salah, F.Z. Meghlaoui, *Study of adsorption of phenol on titanium oxide (TiO_2).* Desalination, 2004. **166**: p. 355.

122. Waite, J.H., *Mussel power.* Nature Materials, 2008. **7**: p. 8.

123. L. Haeshin, S.M.D., W.M. Miller, P.B. Messersmith, *Mussel-Inspired Surface Chemistry for Multifunctional Coatings.* Science, 2007. **318**: p. 426.

124. X. Fan, L.L., P.B. Messersmith, *Surface-initiated polymerization from TiO_2 nanoparticle surfaces through a biomimetic initiator: A new route toward polymer–matrix nanocomposites.* Composites Science and Technology, 2006. **66**: p. 1198.

125. P.Z. Araujo, P.J.M., M.A. Blesa, *Interaction of Catechol and Gallic Acid with Titanium Dioxide in Aqueous Suspensions. 1. Equilibrium Studies.* Langmuir, 2005. **21**: p. 3470.

126. I.A. Jankovic, Z.V.S., M.I. Comor, J.M. Nedeljkovic, *Surface Modification of Colloidal TiO2 Nanoparticles with Bidentate Benzene Derivatives.* Journal of Physical Chemistry C, 2009. **113**: p. 12645.